

The Thermal Structure of Triton's Atmosphere: Results from the 1993 and 1995 Occultations

C. B. Olkin,^{1,2} J. L. Elliot,^{3,4} H. B. Hammel,¹ A. R. Cooray,^{1,4} S. W. McDonald, and J. A. Foust

Department of Earth, Atmospheric, and Planetary Sciences, Massachusetts Institute of Technology, Cambridge, Massachusetts 02139–4307
E-mail: colkin@lowell.edu

A. S. Bosh, M. W. Buie, R. L. Millis, and L. H. Wasserman

Lowell Observatory, Flagstaff, Arizona 86001–4499

E. W. Dunham² and L. A. Young⁵

NASA Ames Research Center, Space Science, Moffett Field, California 94035–1000

R. R. Howell

Physics and Astronomy Department, University of Wyoming, Laramie, Wyoming 82071

W. B. Hubbard and R. Hill

Lunar and Planetary Laboratory, University of Arizona, Tucson, Arizona 85721

R. L. Marcialis⁶

Pima Community College, 2202 West Anklam Road, Tucson, Arizona 85709

J. S. McDonald

SETI Institute, 2035 Landings Drive, Mountain View, California 94043

D. M. Rank and J. C. Holbrook

University of California, Lick Observatory, Santa Cruz, California 95064

and

H. J. Reitsema

Ball Aerospace, P.O. Box 1062, Boulder, Colorado 80306–1062

Received October 11, 1996; revised April 18, 1997

¹ Visiting Astronomer at the Infrared Telescope Facility, which is operated by the University of Hawaii under contract to the National Aeronautics and Space Administration.

² Now at Lowell Observatory, Flagstaff, Arizona.

³ Also at Lowell Observatory, Flagstaff, Arizona.

⁴ Also at Department of Physics, Massachusetts Institute of Technology.

⁵ Now at Department of Astronomy, Boston University, Boston, Massachusetts.

⁶ Also at Lunar and Planetary Laboratory, University of Arizona, Tucson.

This paper presents new results about Triton's atmospheric structure from the analysis of all ground-based stellar occultation data recorded to date, including one single-chord occultation recorded on 1993 July 10 and nine occultation lightcurves from the double-star event on 1995 August 14. These stellar occultation observations made both in the visible and in the infrared have good spatial coverage of Triton, including the first Triton central-flash observations, and are the first data to probe the altitude level 20–100 km on Triton. The small-planet lightcurve model of J. L. Elliot and L. A. Young (1992, *Astron. J.* **103**, 991–1015) was generalized to include stellar flux re-

fracted by the far limb, and then fitted to the data. Values of the pressure, derived from separate immersion and emersion chords, show no significant trends with latitude, indicating that Triton's atmosphere is spherically symmetric at ~ 50 -km altitude to within the error of the measurements; however, asymmetry observed in the central flash indicates the atmosphere is not homogeneous at the lowest levels probed (~ 20 -km altitude). From the average of the 1995 occultation data, the equivalent-isothermal temperature of the atmosphere is 47 ± 1 K and the atmospheric pressure at 1400-km radius (~ 50 -km altitude) is 1.4 ± 0.1 μ bar. Both of these are not consistent with a model based on Voyager UVS and RSS observations in 1989 (D. F. Strobel, X. Zhu, M. E. Summers, and M. H. Stevens, 1996, *Icarus* **120**, 266–289). The atmospheric temperature from the occultation is 5 K colder than that predicted by the model and the observed pressure is a factor of 1.8 greater than the model. In our opinion, the disagreement in temperature and pressure is probably due to modeling problems at the microbar level, since measurements at this level have not previously been made. Alternatively, the difference could be due to seasonal change in Triton's atmospheric structure. © 1997 Academic Press

I. INTRODUCTION

Our knowledge of Triton's lower atmosphere is based on relatively few observations. Spectra observed from Earth reveal the surface ices N_2 , CH_4 , CO, and CO_2 (Cruikshank and Silvaggio 1979, Cruikshank *et al.* 1984, 1993). For a wide range of temperatures, these species would coexist as vapor and ice. N_2 is the major atmospheric constituent, because it has the greatest vapor pressure at the temperature of 38 ± 1 K inferred from the band shape of N_2 (Tryka *et al.* 1993) and the Voyager IRIS measurements (Conrath *et al.* 1989). Two of the species, N_2 and CH_4 , were directly detected as gases by the Voyager UVS solar and stellar occultations, while an upper limit of 0.01 was placed on the mixing ratio of CO (Broadfoot *et al.* 1989). These UVS occultation data also determined the N_2 temperature at an altitude of 475 to 675 km to be 102 ± 3 K (Krasnopolsky *et al.* 1993). Voyager 2 images show dark plumes rising from the surface and leveling off at an altitude of 8 km (Soderblom *et al.* 1990). Clouds and haze were detected below 30-km altitude (Smith *et al.* 1989; Pollack *et al.* 1990).

The most direct probes of the lower atmospheric structure are the two occultations of the Voyager spacecraft radio signal by Triton as seen from Earth (Tyler *et al.* 1989, Gurrola 1995). The phase shift in the radio signal directly yields the refractivity of the atmosphere as a function of radius, which can be converted to a number density profile if one knows the mix of gases. Finally, one can obtain temperature and pressure profiles if one assumes the atmosphere is in hydrostatic equilibrium. Since the phase shift of the radio signal was small in the neutral atmosphere,

the analysis of the RSS results was based on model fitting, rather than numerical inversion, and the surface pressure was found to be 16 ± 3 μ bar (Tyler *et al.* 1989), later refined to 14 ± 1 μ bar (Gurrola 1995). Another relevant result of the RSS occultations is a determination of Triton's surface radius, 1355 ± 7 km (Tyler *et al.* 1989), which can be compared with the value of 1352.6 ± 2.4 km derived from measurements of the Voyager images (Davies *et al.* 1991).

Models of the pressure and temperature as a function of altitude for Triton's atmosphere make the implicit assumption that the atmosphere is substantial enough that the surface ice is maintained at a constant temperature through buffering by sublimation and condensation (Trafton 1984, Ingersoll 1990, Yelle *et al.* 1995). Given this assumption, one can use atmospheric measurements from different locations on Triton to constrain a single atmospheric model of the vertical temperature and pressure profiles. Models by Strobel and Summers (1995), Krasnopolsky *et al.* (1993), and Strobel *et al.* (1996) determine the vertical atmospheric structure above the tropopause from radiative–conductive calculations, which include the effects of CH_4 heating and cooling, CO cooling, magnetospheric electron heating, and solar EUV heating. Broadly speaking, the resulting thermal profile begins at the surface temperature of 38 K, drops adiabatically to 37 K at an altitude of 8 km (following the troposphere model of Yelle *et al.* 1991), then rises smoothly to 102 K at 600 km.

Given our current state of knowledge of Triton's atmosphere, we set out to (1) probe Triton's atmosphere in the microbar pressure region where previous observations do not exist and compare with model predictions, (2) investigate seasonal change which has been predicted based on the vapor-pressure equilibrium of Triton's atmosphere with the surface ices, and (3) investigate spatial variability with a multi-chord occultation observation. These tasks require high-resolution information about Triton's atmospheric structure, and at present this information can be acquired from Earth only through observation of a series of stellar occultations. We began such observations in 1993, with the successful Kuiper Airborne Observatory (KAO) observation of the occultation of the star Tr60, $R = 13.9$ (McDonald and Elliot 1992), by Triton. On 1995 August 14, nine additional chords were obtained from six sites during the occultations of Tr148A and Tr148B including combined visible and IR observations from two sites, observations of both occultations at two sites, and the observation of the central flash for Tr148B from the IRTF. These data probe an altitude range near the microbar pressure level (20–100 km of altitude) intermediate to those sensed by Voyager's instruments.

In this paper the entire ground-based stellar occultation data set (Tr60, Tr148A, and Tr148B) is used to address the goals described in the previous paragraph by fitting

the lightcurve model of an isothermal atmosphere (with an optional power-law thermal gradient) developed for Pluto by Elliot and Young (1992).

II. PREDICTION OF THE GROUND TRACKS

The occulted stars, Tr60 and Tr148, were identified in an observational program to search for Triton occultation candidates (McDonald and Elliot 1992, 1995). Since the error in these initial predictions was estimated to be ± 0.25 arcsec (equivalent to nearly the diameter of the Earth subtended at the Earth–Triton distance), further observations of Triton and the stars were needed to improve the predictions, to deploy observers within the ground tracks of the occultations. Triton’s radius subtends an angle of about 0.07 arcsec as seen from the Earth, so our final accuracy goal, to place the KAO within the shadow with confidence, was ± 0.02 arcsec.

Refinement observations for occultation predictions are most effective when both bodies involved in the occultation can be recorded on the same CCD strip scan or stare frame, such that (unknown) differences between the coordinate systems of the stellar reference network and the body ephemeris will not affect the relative positions. Our reduction procedure, when both bodies are on the same frame, allows for the transformation between the local stellar and ephemeris coordinate systems to include an offset, rotation, and scale factor. For a discussion of our methods used to reduce and analyze the prediction-refinement observations, see Olkin (1996).

Tr60 Prediction

We planned three data sets that would record both bodies on the same scan or frame: (1) strip scans with the SNAPSHOT clone on the 0.9-m Crossley Telescope at Lick Observatory (Dunham *et al.* 1985, Dunham 1995); (2) strip scans with SNAPSHOT (Dunham *et al.* 1985) on the 0.61-m telescope at the George R. Wallace, Jr., Astrophysical Observatory, and (3) stare frames recorded with the CCD camera on the 1.6-m astrometric reflector at the U.S. Naval Observatory (USNO) Flagstaff Station. Limited by the amount of sky that could be exposed on a single strip scan or stare frame, the Lick and Wallace observations began about 8 weeks before the event. The USNO observations began just 3 days prior to the event and were used to make the final adjustment in the KAO flight plan. The final prediction based on the USNO observations gave a geocentric impact parameter of 0.04 ± 0.02 arcsec, which is within one standard deviation of the post-event value: 0.026 ± 0.006 arcsec (see Fig. 1).

Tr148 Prediction

Only from the occultation observations did we learn that Tr148 had two components, since the two stars, Tr148A

and Tr148B, appear blended in Earth-based imaging. Thus, our prediction was based on center-of-light observations of the pair. With the initially predicted closest approach distance of 0.42 arcsec (McDonald and Elliot 1995), the occultation would not be visible from Earth; however, 7 months before the occultation, astrometric observations of Tr148 (the blended star image) by the Carlsberg Automatic Meridian Circle (CAMC) yielded a geocentric closest approach distance between the star and Triton of 0.30 ± 0.13 arcsec (CAMC star position: J2000 $\alpha = 19^{\text{h}}41^{\text{m}}00^{\text{s}}.376$; $\delta = -20^{\circ}51'41''.20$, B. Argyle, personal communication). This prediction placed the centerline of the occultation shadow tangent to Earth’s limb with an error in the prediction equal to the diameter of Triton as seen from Earth.

The prediction was further refined with both stare frame and strip scan observations. From 52 stare frames recorded at the USNO on 2 nights before the occultation, the predicted geocentric closest approach of the center of Triton to the blended stellar image was 0.31 ± 0.05 arcsec. From strip scans recorded at Lick Observatory’s Crossley telescope (150 observations of Triton and 154 of the blended Tr148A–Tr148B image) the predicted closest approach was 0.28 ± 0.02 arcsec. For comparison, the reconstructed shadow path, from the multiple chord occultations (see Section VI), yielded geocentric impact parameters of 0.2788 ± 0.0003 arcsec for Tr148A and 0.1961 ± 0.0012 arcsec for Tr148B. The corresponding shadow paths are displayed in Fig. 2.

To compare the predicted and reconstructed impact parameters, we converted the reconstructed results into a center-of-light prediction for the pair. Using the Tr148A/Tr148B intensity ratio of 4.19 (Section VIII) from unfiltered visual wavelength observations of both occultations from one station, we calculated the center-of-light reconstructed prediction to be 0.247 ± 0.002 arcsec, about 1.5 standard deviations smaller than the weighted prediction from the Lick and USNO data.

III. TR60 OBSERVATIONS

Observations of the Tr60 occultation were attempted from western Australia at Perth Observatory, South America at Cordoba Astronomical Observatory, South Africa at the South African Astronomical Observatory, and the South Atlantic from the KAO. A telescope at each of these sites was equipped with a portable CCD (PCCD) occultation photometer (Buie *et al.* 1993), the first joint deployment of these four instruments. These observations were unfiltered to maximize the signal-to-noise ratio (SNR) of the lightcurves. Table I gives specifics of all Triton occultation observations recorded (or attempted) to date. Subframe size and detector scale are reported in binned pixels for those observations recorded with on-chip binning. For datasets with lightcurves derived from aperture

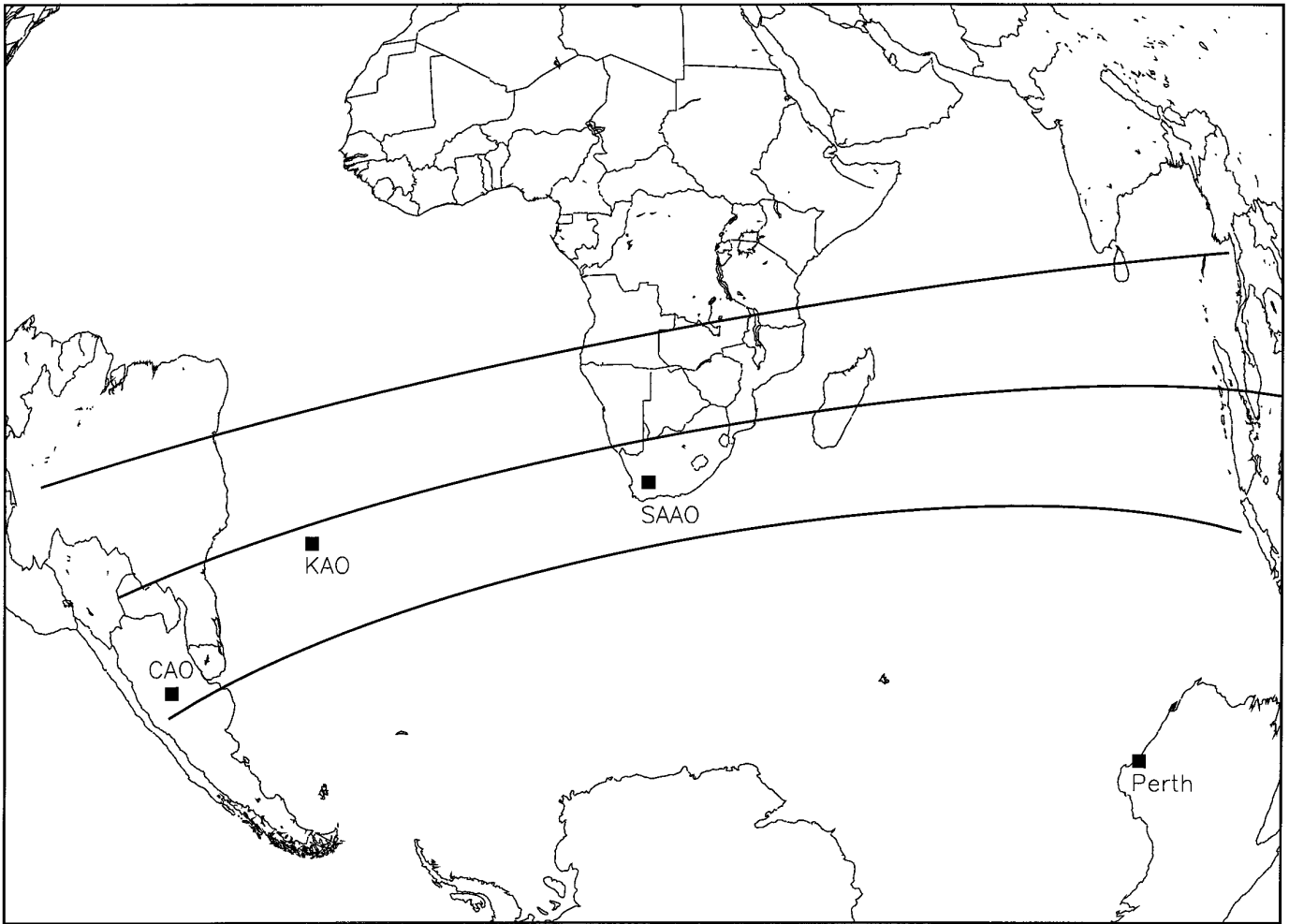


FIG. 1. Mercator projection of Earth showing the observing station locations and a posteriori estimate of the Tr60 occultation shadow path which was determined from imaging data taken before and after the event at the 1.6-m USNO Flagstaff Station (geocentric impact parameter of 0.026 ± 0.006 arcsec). The three lines of the shadow path are the northern limit, midline, and southern limit assuming a shadow radius of 1448 km. Australia was south of the occultation shadow. The path crossed South Africa and Argentina, but clouds prevented the observations. The event occurred near opposition when most of the Triton-facing hemisphere of Earth was in darkness.

photometry, the aperture size is given; for those reduced using numerical point-spread function (PSF) photometry, the full width at half-maximum (FWHM) of the PSF is given. The SNR in a 1-sec integration is derived from the scatter in the isothermal model fit residuals.

Since the skies in South Africa and South America were cloudy and the occultation path passed north of observers in Australia, the only observed occultation chord was recorded from the Kuiper Airborne Observatory. The KAO was deployed from Punta Arenas, Chile, due to the expected southern track of the occultation shadow; intermediate predictions had put the shadow path as far south as the southern tip of South America. As we received new astrometric measurements, the predicted shadow path was

refined, and each day the updated prediction consistently moved the shadow north. This complicated the deployment plans as we needed the full flight range of the KAO to get to the occultation shadow.

Sample frames of the KAO observations are displayed in Fig. 3. We could not use aperture photometry to derive the lightcurve from the images because of the proximity of Neptune to the blended Triton–Tr60 and the rapidly changing image shape (due to the telescope tracking). To get the highest SNR lightcurve, we used a numerical PSF model fitting method to determine the intensity of the blended Triton–Tr60 image relative to Neptune. A field star brighter than the blended Triton–Tr60 image would have been the best choice as a reference PSF. Unfortu-

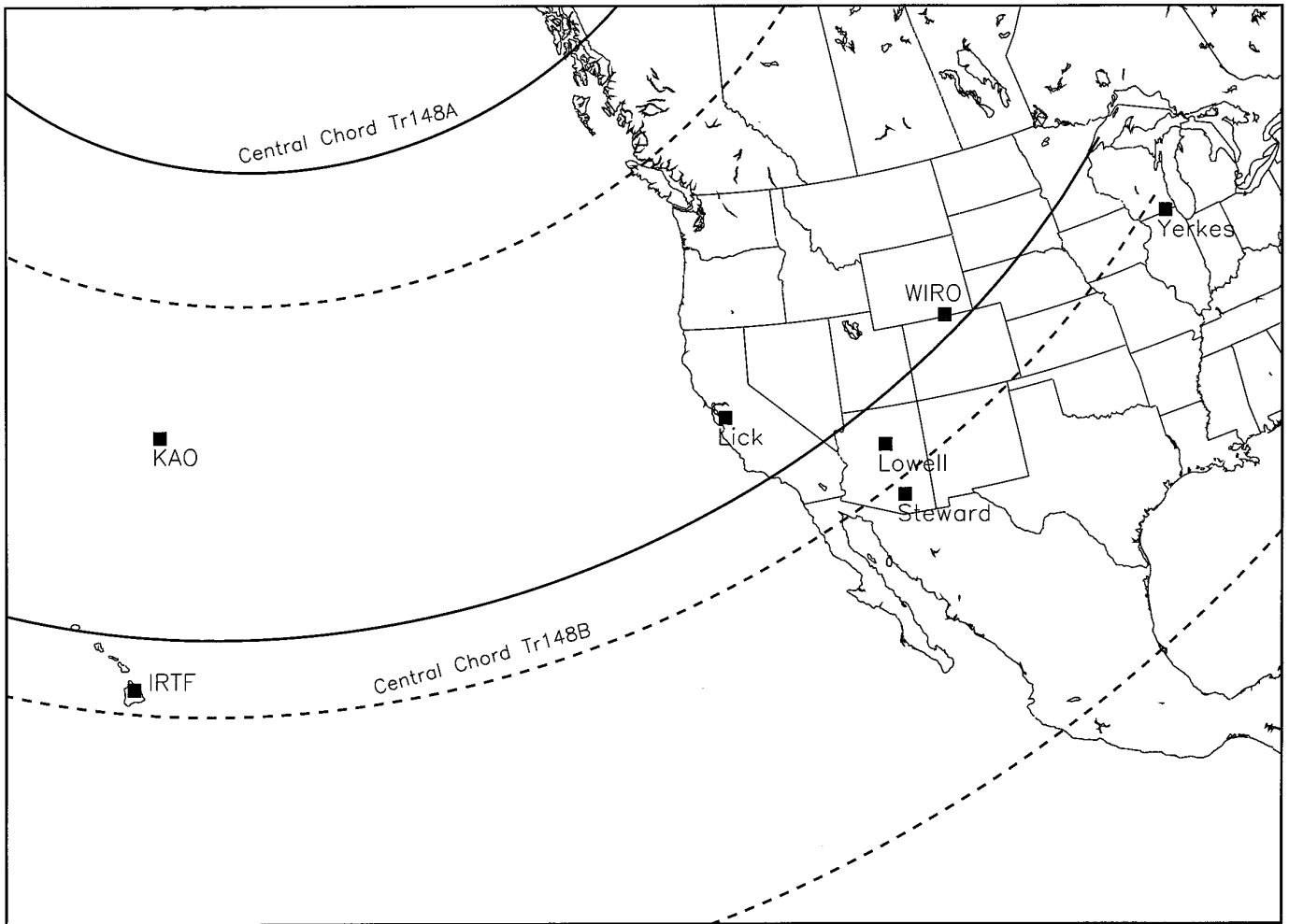


FIG. 2. Mercator projection of Earth showing the observing station locations and a posteriori estimate of the shadow path for the Tr148A (solid line) and Tr148B (dashed line) occultations. The occultation of both stars was recorded at two sites from Lick Observatory. Observers on the KAO and at WIRO recorded the occultation of the brighter star only, while observers at the IRTF and Lowell Observatory recorded the occultation of the fainter star only. Observations of the Tr148B occultation at WIRO and Steward Observatory were compromised by clouds, and those at the KAO, by instrumentation problems. The Hubble Space Telescope was south of both shadow paths.

nately, no such star was available, so Neptune was used. Although Neptune is not a point source (its disk subtends 2.3 arcsec), we can use it as a PSF source because of the 3- to 5-arcsec seeing on the KAO. Other PSF fitting techniques, such as using an analytic model, i.e., an elliptical Lorentzian (Bosh *et al.* 1992), proved unsatisfactory because the frequently elongated PSF was not well fit by the analytic model. Our method provided an error in the ratio for each subframe, which was used to weight the data in the fits to the occultation lightcurves.

A model numerical PSF for each frame was derived from a cubic interpolation of the Neptune image with the background removed. After each iteration, the background was recalculated and the numerical PSF model was updated (by removing the new background). A two-source

image model was fit simultaneously to the blended image of Triton–Tr60 and the image of Neptune. The fitted parameters include an offset of the Triton–Tr60 center from Neptune, the ratio of the peak of the Triton–Tr60 PSF relative to the Neptune PSF peak, and three background parameters (a mean level, row slope, and column slope). Pixels common to both PSFs were not included in the fit.

IV. TR148 OBSERVATIONS

Nine lightcurves were derived from the two occultations in 1995. The four PCCD instruments were set up at the Infrared Telescope Facility on Mauna Kea (MIT system), aboard the KAO (NASA Ames system), at the 1.8-m telescope at Lowell Observatory (Lowell system), and at the

TABLE I
Observational Parameters

Star	Observatory	Telescope aperture (m)	Instrument	Int. time (s)	Dead time (s)	Subframe size (pixels)	Detector scale (arcsec/pix)	No. integrations	Aperture size (arcsec)	FWHM of ref. PSF (arcsec)	SNR per sec	Observers	Comments
Tr60	KAO	0.9	Ames PCCD	0.50	0	50×50	1.0	4200	-	3-5	17.4	Elliot, Dunham & Olkin	
Tr60	Perth	0.6	Lowell PCCD	-	-	-	-	-	-	-	-	Wasserman, Birch	Track north of telescope.
Tr60	CAO	1.5	U. of A. PCCD	-	-	-	-	-	-	-	-	Hubbard, Reitsema, Carranza	Cloudy
Tr60	SAAO	1.0	MIT PCCD	0.50	0	40×40	-	5000	-	-	-	Millis, Bus	Cloudy
Tr148B	IRTF	3.0	MIT PCCD	0.30	0	23×23	0.3	8000	4.8	-	46.8	Olkin, Hammel, Cooray	
Tr148B	IRTF	3.0	NSFCAM	0.50	0.024	48×48	0.31	3600	3.7	-	16.5	Olkin, Hammel, Cooray	
Tr148A	KAO	0.9	Ames PCCD	0.342	0	50×50	1.0	3600	-	3-5	27.0	Elliot, Dunham	
Tr148A	Lick	0.9	SNAPSHOT	1.00	0	40×40	1.14	1800	8.0	-	24.2	McDonald, Young	
Tr148B	Lick	0.9	SNAPSHOT	1.00	0	40×40	1.14	1800	8.0	-	5.8	McDonald, Young	
Tr148A	Lick	1.0	LIRC2	3.00	3-12	256×256	1.14	260	4.6	-	9.5	Rank, Holbrook	
Tr148B	Lick	1.0	LIRC2	3.00	3-12	256×256	1.14	260	4.6	-	2.0	Rank, Holbrook	
Tr148B	Lowell	1.8	Lowell PCCD	0.14	0	46×30	0.59	9400	3.5	-	9.4	Buie, Millis, Wasserman	
Tr148A	WIRO	2.3	U. of A. PCCD	0.40	0	90×50	3.25	3000	-	3.25	7.2	Reitsema, Hill, Howell	Track north of telescope.
Tr148	HST	2.4	FOS	0.20	-	-	-	4437	-	-	-	Bosh	
Tr148	Steward	2.2	2-channel photometer	-	-	-	-	-	-	-	-	Hubbard, Marcialis	Cloudy
Tr148	Yerkes	1.1	CCD	3.	3	252×241	0.6	117	8.4	-	-	Wild, Briggs, Drish	No occultation in data

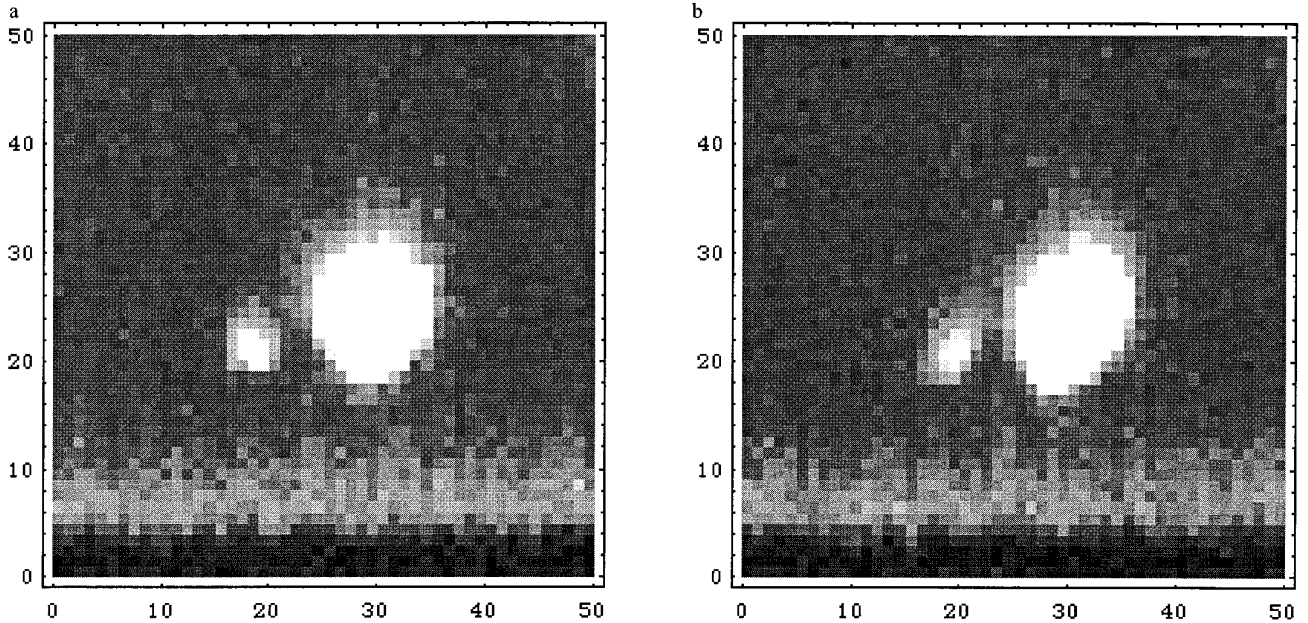


FIG. 3. Sample images from the Triton occultation of Tr60. In both images there are two sources. The brighter object is Neptune; the other (lower and to the left) is the blended image of Triton–Tr60. (a) shows a “round” point-spread function (frame 1803), while (b), taken just 1.0 sec later, shows a “trailed” point-spread function (frame 1805). A charge transfer efficiency problem is seen by the streaking of the images toward the top. The bright band in the lower 10 rows of the subframe is an artifact of the detector readout. The image scale is approximately 1 arcsec/pixel. At this time, Triton was near eastern elongation and ~ 15 arcsec from Neptune.

Wyoming Infrared Observatory (University of Arizona system). At the 0.9-m Crossley telescope at Lick Observatory, a SNAPSHOT clone (Dunham *et al.* 1985) was used to record high-speed images of the occultation. This instrument, like the PCCD, was designed for high-speed occultation observations, and the integrations are triggered from a GPS signal. All the visible wavelength observations were recorded unfiltered. The lightcurve of the blended Triton–Tr148 from Lowell Observatory was divided by the lightcurve from Neptune to remove any varying extinction.

Two infrared instruments were also used: (1) NSFCAM (Shure *et al.* 1994) at the IRTF, and (2) LIRC2 at the 1.0-m telescope at Lick Observatory. The NSFCAM observations were recorded with a K filter (center wavelength = $2.21 \mu\text{m}$, FWHM = $0.39 \mu\text{m}$) and the LIRC2 with a K' filter (center wavelength = $2.12 \mu\text{m}$, FWHM = $0.34 \mu\text{m}$). For comparison, the effective wavelength of the IRTF-visible wavelength data is $\sim 0.7 \mu\text{m}$. NSFCAM has subframe readout capabilities to reduce deadtime, but does not have a frame transfer scheme. To establish the deadtime for NSFCAM, which depends on the number of pixels being read out and the location of those pixels, images of an infrared light-emitting diode blinking once per second, triggered by a GPS receiver, were recorded in occultation mode (same box size, box location, integration time, and series length as the occultation observations). The deadtime for these observations is 24 msec. With the LIRC2, full frame images were recorded, and the deadtime between

integrations, while the detector was being read out, is several seconds.

At WIRO, clouds of varying optical depth were present throughout the data recording interval. To first approximation, the effect of clouds was removed from the blended Triton–Tr148A–Tr148B signal by using Neptune as a monitor; however, there is some evidence that the clouds are not completely neutral as a function of wavelength, and color differences between the various signal components may compromise photometric accuracy at some level.

For the KAO observations, the start time of the data recording was triggered from the GPS receiver, but the exposure timing was not, because of a communication problem between the instrument computer and the GPS receiver. As a result, the integration time was controlled by the clock in the instrument computer. The integration time was determined to be 0.342 sec from a series of images of the secondary mirror nodding in and out of the beam at a frequency of 1 Hz controlled by a GPS receiver.

The IRTF lightcurves and their fit results differ from those of Olkin (1996) due to an improved method of aperture photometry used in this work.

V. LOCATION OF THE TR60 OCCULTATION GROUND TRACK

The closest approach distance between Triton and Tr60 was best determined by analysis of pre- and post-event

imaging of the occulted star and Triton recorded at the 1.6-m telescope at the USNO (Olkin *et al.* 1996). These USNO data give the closest approach of the KAO to the center of Triton's shadow to be 359 ± 133 km. As a test of the astrometric method, Olkin *et al.* (1996) found the occultation midtime derived from the USNO frames is 2.2 ± 4.1 sec earlier than the midtime from the occultation lightcurve itself. The latitudes probed by the occultation lightcurve reported in Olkin *et al.* (1996) are incorrect. Figure 4 depicts Triton's globe and the path of the star as seen from the KAO, as well as the latitudes probed as a function of time.

VI. LOCATION OF THE TR148 OCCULTATION GROUND TRACK

The multiple occultation chords from the Tr148A and Tr148B events were used to reconstruct the occultation shadow path, to determine where on Triton each chord probed, and to establish the separation of the double star. First, we defined the shadow plane, also known as the fg plane (Elliot *et al.* 1993), to be perpendicular to the line-of-sight to the star, such that the perpendicular to the fg plane points to the occulted star (using coordinates of the blended star as determined by the CAMC), \hat{f} points in the direction of increasing right ascension, and \hat{g} completes the right-handed system (increasing declination). An offset of each star from the blended center, (f_{0A}, g_{0A}) and (f_{0B}, g_{0B}) , is determined by fitting the positions of the observers relative to the shadow center (f_{pr} and g_{pr}) at the immersion and emersion half-light times to a model for Triton's figure. The offsets account for errors in the star position and/or Triton's ephemeris.

The positions of the observers relative to the shadow center are determined by Triton's ephemeris and the coordinates of the observers. The DE211 ephemeris and the NEP016 model (Jacobson *et al.* 1991) were used to calculate a light time-corrected J2000 Triton ephemeris. The ephemeris was converted from right ascension, declination, and distance to the shadow plane coordinates $f_p(t)$ and $g_p(t)$. Next, the position of the observer (receiver) in the shadow plane $f_r(t)$ and $g_r(t)$ was calculated from the geodetic coordinates of the observing site (Table II). For the occultation of Tr148A, the position of the observer relative to the shadow center at a time t is given by

$$\begin{aligned} f_{pr}(t) &= f_r(t) - (f_p(t) - f_{0A}), \\ g_{pr}(t) &= g_r(t) - (g_p(t) - g_{0A}); \end{aligned} \quad (1)$$

an analogous equation exists for the Tr148B occultation data. These coordinates at the immersion and emersion half-light times were used in a fit of Triton's figure. The

immersion and emersion times at half-light were derived from fits to the occultation lightcurves using an isothermal model (see Table II). The lightcurve model is an extension of Elliot and Young (1992) to include the flux contribution from the far limb and is presented in Section VII.

The parameters of the least-squares fit include the star offsets and parameters describing Triton's figure (i.e., semi-major axis, ellipticity, and orientation angle). These parameters are adjusted to minimize the distance between the location probed at half-light and the figure of Triton along the direction of the shadow path. The orientation of the semimajor axis of Triton's figure is measured from the f axis (positive angle measured from g to f). Because the lightcurves are of different quality, the fits were weighted with the formal errors from the half-light timings. The fitted parameters and their formal errors are given in Table III for two different models: circular figure and elliptical figure.

We refit the lightcurve timings to a circular figure of Triton without the IRTF observations (since they control the weighted fit) to see how robust the solution is. The two solutions (circular figure with and without the IRTF timings) agreed within their errors, and the impact parameter for the IRTF differed from the adopted solution by only 6 km (much less than 1σ). Unlike the circular-figure fits, varying the data in the oblate-figure fits affects the results. We chose the circular-figure model as our adopted solution because of its robustness. The declination offsets (g_{0A} and g_{0B}) of the two stars in the adopted solution are systematically north of the CAMC position (used as the reference in this system). This could be due to (1) an error in the Triton ephemeris, (2) an error in the CAMC measurement, (3) a disagreement between the coordinate systems of the star's coordinate and the ephemeris, or (4) all the above.

From the Faint Object Spectrometer (FOS) on the Hubble Space Telescope, we have a resolved "image" of the double star, exposed on the day of the occultation. Although the FOS is a one-dimensional array detector, "images" are constructed by moving the stellar source perpendicular to the detector array to add the second dimension. We have fit a two-source PSF model to the image to determine the separation of Tr148A and Tr148B. The separation is either greater or less than that derived from the occultation timings (Table III), depending on the choice of reference PSF. Therefore, these data are consistent with the results from the occultation timings, but cannot provide a more precise estimate of the star's separation.

From the fit results of Table III and the locations of the observers, we determine the impact parameter (ρ_{min}), which is the closest distance between the observer and the center of the occultation shadow (see Table IV). Also included in the table is the residual for each site (the distance along the shadow path between the position probed at half-light and the figure) and the velocity of the occulta-

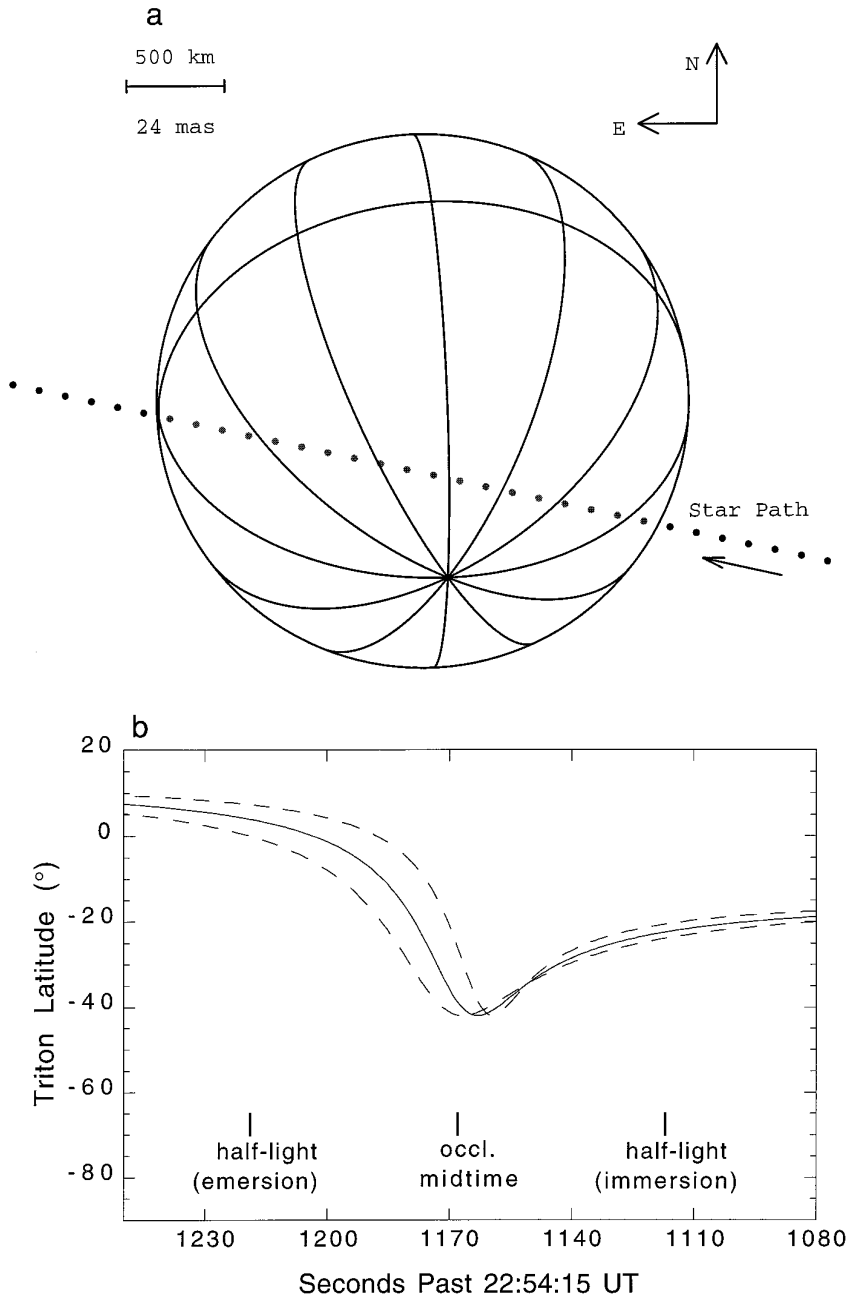


FIG. 4. Locations on Triton probed by the stellar occultation of Tr60. (a) Path of the star at 5-sec intervals as it is occulted by Triton. The scale bar indicates 500 km or 24 milliarcsec. The uncertainty in the star path is about 6 milliarcsec. (b) Latitudes probed by the near limb as a function of time. The dashed lines indicate $\pm 1 \sigma$ uncertainty in the path. The time axis is reversed to be consistent with (a). The occultation midtime and immersion/emersion half-light times are indicated.

tion shadow relative to the observer (the shadow velocity). The longitudes and latitudes probed on Triton by each chord at the time of half-light are given in Table V (derived from Triton's pole and prime meridian from Seidelmann 1992). The astrometric solution is depicted in Fig. 5, with a globe of Triton as seen from Earth at the event time.

The perpendicular distance between the extreme occultation chords spans 2013 km on Triton (74% of the globe; from the Lick Tr148B chord 706 km north of Triton's center to the WIRO chord 1307 km south of Triton's center). The mean separation between chords is ~ 400 km, which is good spatial coverage for a small-body occultation.

TABLE II
Geodetic Observatory Coordinates from GPS (WGS84) and Half-Light Times

Site	Longitude ($^{\circ}$: $'$: $''$)	σ (Longitude) (arcsec)	Latitude ($^{\circ}$: $'$: $''$)	σ (Latitude) (arcsec)	Altitude (m)	σ_{alt} (m)	Half-light times UT (mm:ss) after		Timing error (s)
							1995 08 14 07 hr immersion	emersion	
IRTF	-155:28:20.	2.0	19:49:34.	3.0	4182.	75.	33:16.29	35:09.81	0.08
KAO (immersion)	-157:30:50.	1.0	32:36:10.	1.0	13004.	30.	38:37.00	40:17.96	0.14
KAO (emersion)	-157:42:55.	1.0	32:32:28.	1.0	12949.	30.	38:37.00	40:17.96	0.14
Lick (Tr148A)	-121:38:38.9	0.2	37:20:17.7	0.2	1241.	7.	36:41.97	37:56.42	0.21
Lick (Tr148B)	-121:38:38.9	0.2	37:20:17.7	0.2	1241.	7.	31:08.60	32:46.86	0.79
Lowell	-111:32:10.6	0.2	35:05:48.7	0.3	2209.	5.	30:28.78	32:21.91	0.36
WIRO	-105:58:38.1	0.6	41:05:50.0	0.6	2956.	21.	36:13.67	37:01.18	0.74

TABLE III
Astrometric Solution from Lightcurve Timings for Tr148

Parameter	Circular figure	Elliptical figure
Equatorial radius, km ^a	1427.9 \pm 3.5	1432.6 \pm 5.7 ^a
Ellipticity	0.	-0.029 \pm 0.016
Position angle, deg ^b	0.	70.3 \pm 10.1
f_{0A} , km	2330 \pm 3	2316 \pm 9
g_{0A} , km	-12 \pm 6	23 \pm 22
f_{0B} , km	-5157 \pm 6	-5146 \pm 9
g_{0B} , km	-3385 \pm 29	-3431 \pm 38
Tr148A-Tr148B separation, arcsec	0.3869 \pm 0.0012	0.3874 \pm 0.0011
Position angle of Tr148B from Tr148A, deg ^c	65.75 \pm 0.16	65.16 \pm 0.14
Sum of squared residuals	1504	707
Degrees of freedom (dof)	7	5
Weighted RMS residual per dof	14.7	11.9

^a This is the equatorial radius at half light in the shadow plane which is one scale height smaller than the equatorial radius in the planet plane due to refraction. For the elliptical figure, the semiminor axis is given (-19.7 \pm 10.1 degrees from the equatorial radius).

^b position angle of semimajor axis measured from f , positive in the direction of g to f , which corresponds to North through East on the sky.

^c position angle of Tr148B relative to Tr148 measured from North, positive in the direction of North to East.

TABLE IV
Adopted Astrometric Solution for Tr148

Site	Star	Impact parameter km	Immersion residual, km	Emersion residual, km	Velocity km/s
IRTF	Tr148B	144.5 ± 27.3	0.8	-0.1	25.03
KAO	Tr148A	680.2 ± 5.4	-2.5	5.0	24.80
Lick	Tr148A	1086.6 ± 5.4	0.8	-3.8	24.95
Lick	Tr148B	702.8 ± 27.3	-13.8	20.7	24.95
Lowell	Tr148B	261.0 ± 27.3	-2.1	-13.8	24.92
WIRO	Tr148A	1304.1 ± 5.4	-5.9	-24.7	24.88

VII. THE LIGHTCURVE MODEL

Elliot and Young (1992) describe the processes that affect the observed flux of an occulted star, and we expand their development to explicitly include the far-limb flux contribution (which was not necessary for Pluto). For more discussion of the stellar occultation technique as applied to planetary atmospheres, see the review article by Elliot and Olkin (1996). The basic process is depicted in Fig. 6. Parallel rays of starlight are incident on the planet from the left, with the observer located in the shadow plane a distance D from the planet plane. Both the shadow plane and planet plane are perpendicular to the incident light rays (which are parallel to the x axis). The coordinate r is the radius in the planet plane measured from the center of the occulting body. The coordinate y is the observer's location in the shadow plane; the absolute value of y is the shadow-plane radius ρ . As seen in Fig. 6, the observer can receive flux from two regions of the limb: the near and the far. The near-limb flux received by the observer at y

has not crossed the x axis, whereas the far-limb flux has been refracted across the x axis.

Starlight with a closest approach to the planet r is bent by the refraction angle $\theta(r)$, measured negative toward the planet. At any point in the atmosphere, the light ray is a distance r' from the center of the planet where $r'^2 = r^2 + x^2$. We have assumed the refraction angle is small ($\theta \ll 1$).

The planet-plane radius r is related to the shadow-plane radius ρ by the refraction angle θ and the distance from the observer to the planet D :

$$\begin{aligned} y(r) &= r + D\theta(r), \\ \rho(r) &= |y(r)|. \end{aligned} \quad (2)$$

The starlight at the observer is dimmed by (1) spreading of the light due to refraction and (2) extinction (scattering and/or absorption) of the starlight with line-of-sight optical depth τ_{obs} . The observed flux is also affected by geometric focusing, which is most significant near the center of the

TABLE V
Triton Longitude and Latitude Probed at Half-Light by Tr148

Site	Star	Immersion		Emersion	
		Longitude (deg.)	Latitude (deg.)	Longitude (deg.)	Latitude (deg.)
KAO	Tr60	74.0	-22.5	231.1	3.9
IRTF	Tr148B	81.9	-6.0	270.9	13.5
KAO	Tr148A	110.4	-27.0	244.6	-8.9
Lick	Tr148A	132.4	-36.5	227.5	-22.0
Lick	Tr148B	63.6	9.8	291.7	27.7
Lowell	Tr148B	78.2	-2.8	274.5	16.3
WIRO	Tr148A	153.0	-40.6	212.8	-30.5

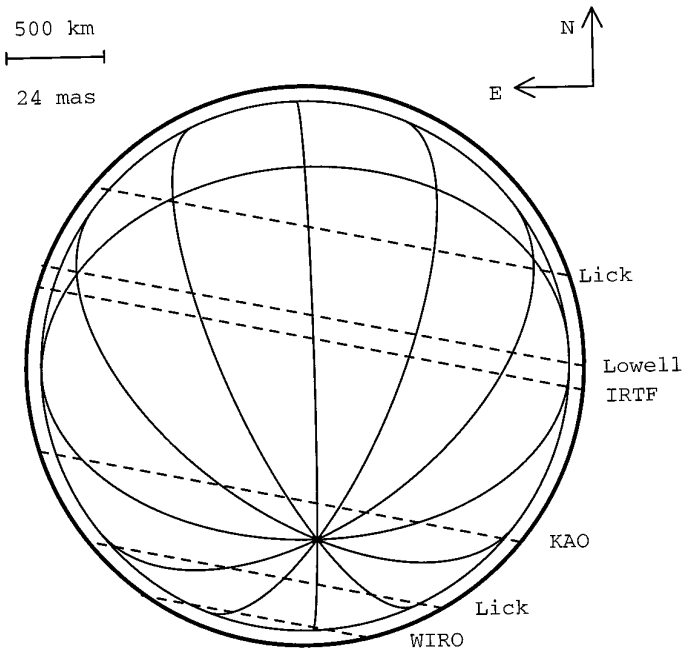


FIG. 5. Triton's globe with the six occultation chords. The three northernmost chords were occultations of the fainter star, Tr148B, and the three southernmost chords were occultations of Tr148A. The outer circle describes the fitted half-light radius (1427.9 km) in the shadow plane, about one scale height smaller than the half-light radius in the planet plane due to refraction (Baum and Code 1953). The scale bar indicates 500 km or 24 milliarcsec.

shadow; the starlight is focused by the ratio of the planet-plane radius to the shadow-plane radius $r/\rho(r)$ as the light at r is compacted into a smaller circumference (radius ρ) due to refraction. From Elliot and Young (1992) we have the following equation for the flux received by the observer from the near limb of a spherical planet $\zeta(r)$:

$$\zeta(r) = \frac{r}{\rho(r)} \left| \frac{dr}{d\rho(r)} \right| e^{-\tau_{\text{obs}}(r)}. \quad (3)$$

Using a radiative–thermal conduction model of atmospheric structure for Triton (Strobel *et al.* 1996; hereinafter S96), we find the product $D\theta$ is greater than the surface radius for the deepest levels probed by the stellar occultations. Therefore, the observer will record flux from both the near and far limbs unless there is extinction sufficient to completely absorb and/or scatter the flux.

Now that we have expressions for $\zeta(r)$ and $y(r)$, we can formulate the observed flux from both limbs. The observed flux from the near limb as a function of y is $\zeta(y) = \zeta(r[y])$. For a spherically symmetric atmosphere, the far-limb flux at y is equal to the near-limb flux at $-y$, and the observed flux from both limbs $\phi(\rho)$ is

$$\phi(\rho) = \zeta(y) + \zeta(-y). \quad (4)$$

If the body is oblate and ρ is small enough, the observer is within the evolute of a central flash (Elliot *et al.* 1977) and there are more contributions to the observed flux (flux is received from all four perpendicular limb points). We do not address the flux within the evolute, since none of the chords probed within the evolute.

The fitted parameters in the lightcurve model include the full-flux level—the combined light from the occulted star and occulting body. For the Tr148A occultations, this also includes the light from Tr148B, since they are unresolved in ground-based imaging. Similarly, for the Tr148B events, the full-flux level includes the light from Tr148A. Another model parameter, the background-flux level, corresponds to the full-flux level without the contribution from the occulted star. A linear slope centered on the midtime of the occultation is included in the lightcurve model. These parameters are defined in Elliot and Young (1992); the units of the background and full levels are sec^{-1} and for the slope it is sec^{-2} .

The remaining parameters are the half-light radius, r_h , and energy ratio, λ_h (gravitational potential energy: kT). The ratio of these two parameters (r_h/λ_h) equals the scale height at the half-light radius, $H(r_h)$, for an isothermal atmosphere. To calculate the model lightcurve, we need

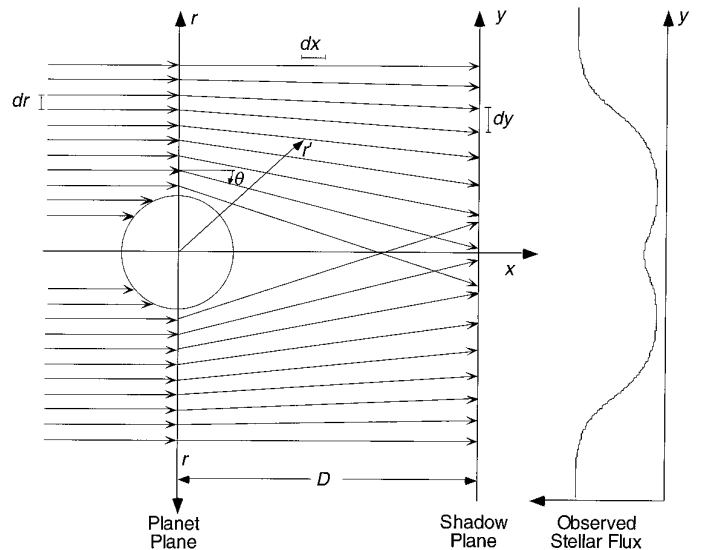


FIG. 6. Stellar occultation by a planetary atmosphere where refraction bends the light rays. The refracted light, dimmed by the spreading of the rays, is observed in the shadow plane. Light that has crossed the x axis (from where the observer is) constitutes the far-limb flux. The resulting occultation lightcurve is seen on the left. The observed signal is the sum of all flux at the observer's location. At some locations this comes from one ray; closer to the center of the shadow path there will be two rays (from the near and far limbs); and even closer the observer is within the evolute of the central flash and there will be more rays contributing to the observed flux. (Reproduced, with permission, from Elliot and Olkin, 1996).

TABLE VI
Parameters for Conversion of Fit Results

Parameter	Value	Reference
Geocentric distance to Triton (1993/07/10), AU	29.169	DE211, NEP016
Geocentric distance to Triton (1995/08/14), AU	29.269	DE211, NEP016
Triton mass, kg	2.1398×10^{22}	Anderson <i>et al.</i> 1992
Molecular weight of N ₂ , amu	28.01	
N ₂ refractivity, v_{STP} at 0.7 μm	2.98×10^{-4}	Peck and Khanna 1966
N ₂ refractivity, v_{STP} at 2.2 μm	2.94×10^{-4}	Peck and Khanna 1966

to know the distance from the observer to Triton which we have approximated by the geocentric distance (see Table VI). We assume the atmosphere is composed entirely of N₂. A small fraction of CH₄ and CO will not significantly change the refractivity at standard temperature and pressure. To convert from lightcurve model parameters (r_h , λ_h) to atmospheric temperature and pressure, we used the mass of Triton and the mean molecular weight of the atmosphere given in Table VI. The refractivity was corrected for the actual temperature and pressure.

VIII. LIGHTCURVE FIT RESULTS

Examination of the lightcurves revealed that the two IRTF lightcurves have a central peak offset from the midtime of the occultation. Furthermore, one can see the slope leading up to the central flash is different from immersion to emersion (Fig. 7), indicating that the atmosphere of

Triton near where the central flash is probing is not homogenous. The isothermal model fits assume that the atmosphere is symmetric, and this assumption is most critical near the midtime of the occultation when a wide range of Triton's limb is being probed. Thus, the asymmetry in the central-flash lightcurves motivated us to perform two different fits to the data. Initially the whole lightcurve was fit; then we repeated the fits to a subsection of the data that had all points within 20% of the midtime (where 100% is measured between half-light times) removed. The partial lightcurve fits reduce the impact of any asymmetry probed as the starlight swept around Triton's limb. The fitted parameters and their formal errors from these fits are given in Table VII. The upper row of each parameter corresponds to the full lightcurve fit, whereas the lower number comes from the partial lightcurve fits, which excluded data nearest the midtime of the event because this section of the lightcurve is most sensitive to asymmetries in the atmospheric structure as it sweeps over a large section of Tri-

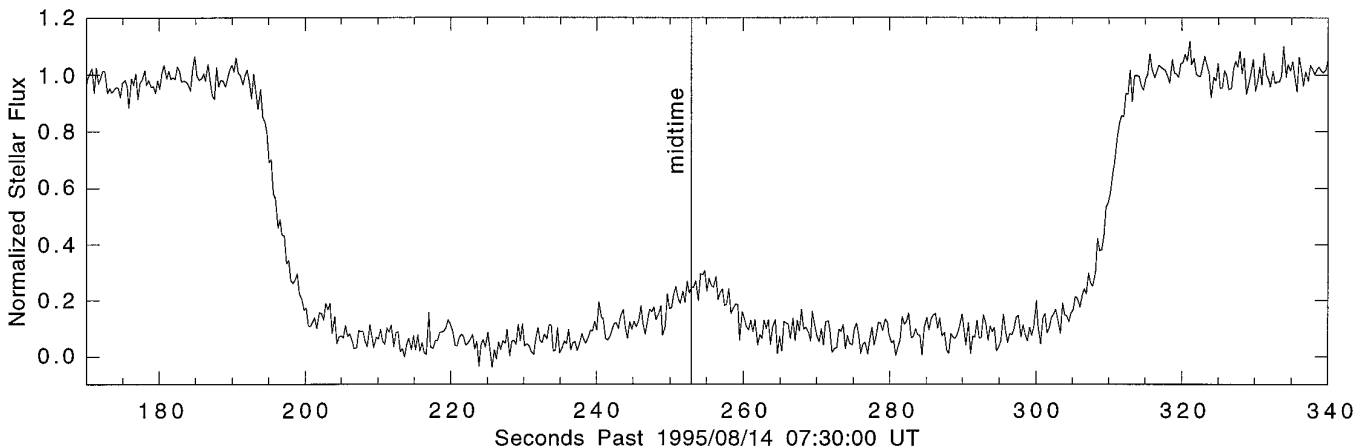


FIG. 7. IRTF (vis) lightcurve with the midtime from the best-fitting isothermal model. The lightcurve demonstrates asymmetry between immersion and emersion in two ways: (1) the peak of the central flash is offset from the midtime determined by the midpoint of the fitted half-light times, and (2) the slope of the central flash is steeper on emersion than immersion. Because of this asymmetry, our adopted fits of the occultation lightcurves do not include data within 20% of the occultation midtime.

TABLE VII
Equivalent-Isothermal Model Parameters from Fits of the Lightcurves^a

Parameter	Light Curve	KAO	IRTF (vis)	IRTF (IR)	KAO	Lick (vis)	Lick (vis)	Lick (IR)	Lick (IR)	Lowell	WIRO
		Tr60	Tr148B	Tr148B	Tr148A	Tr148B	Tr148A	Tr148B	Tr148A	Tr148B	Tr148A
P _{min} (km)		359.	144.5	144.5	680.2	1086.6	702.8	1086.6	702.8	261.0	1304.1
B _{kgd}	full	(160.2 ± 1.3) 10 ⁻⁴	1029120 ± 91	68346 ± 45	(449.5 ± 2.3) 10 ⁻⁴	31068 ± 282	50794 ± 265	485 ± 35	1048 ± 14	(148.3 ± 0.5) 10 ⁻³	0.0 ^c
	partial	(160.6 ± 1.5) 10 ⁻⁴	1029238 ± 104	68522 ± 53	(451.6 ± 3.0) 10 ⁻⁴	30714 ± 425	51299 ± 311			(148.3 ± 0.5) 10 ⁻³	0.0 ^c
Slope	full	(-3.7 ± 1.5) 10 ⁻⁷	0.229 ± 0.170	0.631 ± 0.100	(70.5 ± 6.4) 10 ⁻⁷	0.880 ± 0.600	-1.173 ± 0.412	-0.084 ± 0.012	0.0 ^c	(1.25 ± 1.90) 10 ⁻⁶	0.0 ^c
	partial	(-3.7 ± 1.5) 10 ⁻⁷	0.212 ± 0.170	0.632 ± 0.099	(70.9 ± 6.4) 10 ⁻⁷	0.874 ± 0.607	-1.174 ± 0.416			(1.24 ± 1.90) 10 ⁻⁶	0.0 ^c
Full-flux	full	(2490.9 ± 2.6) 10 ⁻⁵	1050755 ± 26	71903 ± 13	(7745.6 ± 7.9) 10 ⁻⁵	57713 ± 73	57851 ± 61	1213 ± 5.	1212 ± 5	0.1702 ± 0.0002	2.5 ^c
	partial	(2490.9 ± 2.6) 10 ⁻⁵	1050756 ± 26	72053 ± 13	(7745.6 ± 7.9) 10 ⁻⁵	57713 ± 74	57850 ± 62			0.1702 ± 0.0002	2.5 ^c
Mid time ^b	full	321.91 ± 0.15	252.99 ± 0.05	254.05 ± 0.14	567.48 ± 0.09	439.15 ± 0.12	117.38 ± 0.48	434.05 ± 0.24	114.4 ± 1.4	85.37 ± 0.23	397.45 ± 0.51
	partial	321.91 ± 0.15	252.97 ± 0.05	254.00 ± 0.15	567.48 ± 0.09	439.15 ± 0.12	117.45 ± 0.45			85.35 ± 0.24	397.39 ± 0.57
τ _h (km)	full	1450.2 ± 4.0	1447.1 ± 1.2	1441.0 ± 3.6	1446.6 ± 2.1	1449.9 ± 2.0	1448.5 ± 11.0	1455.1 ± 7.7	1448.0 ^c	1452.1 ± 5.8	1460.1 ± 5.8
	partial	1451.0 ± 4.2	1447.7 ± 1.2	1442.9 ± 3.8	1447.0 ± 2.1	1449.2 ± 2.2	1452.8 ± 10.6			1453.5 ± 6.1	1461.1 ± 6.5
λ _h	full	58.6 ± 6.6	74.7 ± 2.4	69.8 ± 6.3	67.5 ± 4.1	71.1 ± 4.8	45.8 ± 11.2	121.6 ± 65.2	69.4 ^c	81.2 ± 16.1	56.0 ± 5.7
	partial	57.5 ± 6.6	74.6 ± 3.0	65.0 ± 7.3	69.1 ± 4.5	67.9 ± 5.1	60.3 ± 18.11			74.9 ± 14.8	51.8 ± 6.5
τ _{min} (km)	full	1365	1372	1362	1378	1395	1378	1417	1380	1380	1423
	partial	1373	1377	1369	1383	1399	1383			1386	1427
dof ^d	full	1114	1495	745	1019	345	444	143	119	1923	159
	partial	1032	1343	658	900	314	403			1599	134

^a Upper number is from full fit; lower is from partial fit, see text.

^b For the Tr60 light curve the midtime is in seconds past 1993/07/10 22:30:00 UTC; for Tr148 it is seconds past 1995/08/14 07:30:00 UTC.

^c Fixed (not fitted) parameters.

^d Number of degrees of freedom in fit.

ton’s limb. Thus, only the main drop and recovery were fit in the partial lightcurve fits to minimize the impact of our assumption of a spherically symmetric atmosphere on the fit results.

Also given in Table VII is the minimum radius probed in the fitted data (r_{\min}). The radius levels probed by the individual lightcurves depend on the impact parameter of the chord and the atmospheric model describing the refractivity of Triton’s atmosphere. Chords probing closer to the shadow center will probe the atmosphere to a lower altitude. At the midtime (for the isothermal atmospheric model in Table VII), the IRTF (vis) lightcurve probed a minimum radius of 1372 km (~ 20 -km altitude). The minimum radius level probed by the IRTF infrared lightcurve differs from the visible dataset by ~ 6 km due to the different isothermal models derived from fitting the two lightcurves.

The occultation lightcurves were normalized with the fitted background level, slope, and full-flux levels and are displayed in Fig. 8. For some of the datasets, only a section of the fitted data is displayed.

From the fit results, we can determine the intensity ratio of Tr148A to Tr148B using the Lick Observatory occultation lightcurves which recorded both events. From the difference in the fitted full-flux level and the background level, the intensity ratio of the two stars is 4.19 ± 0.22 from the unfiltered SNAPSHOT system (similar to an R magnitude, Dunham *et al.* 1991) and 4.44 ± 0.46 from the LIRC2 observations which used a K' filter. From the magnitude of the blended star $V = 12.96 \pm 0.03$ (personal communication from B. Argyle at the CAMC) and $K = 10.98 \pm 0.11$ (Olkin 1996), we get the individual magnitudes of Tr148A ($V = 13.19 \pm 0.03$, $V - K = 1.99 \pm 0.12$) and Tr148B ($V = 14.73 \pm 0.05$, $V - K = 1.93 \pm 0.15$) if we assume the intensity ratio in R equals the intensity ratio in V , and that the ratio in K' is the same as that in K . The $V-K$ colors are consistent with a spectral type of $K0$ (Allen 1973), but if these stars were a physical double, we would expect Tr148B to have a later spectral type than Tr148A because it is fainter.

Next, we address extinction using the fit results. We determined the zero-flux level of the occultation lightcurve and compared it to the fitted value using the intensity ratio from the SNAPSHOT system and post-event photometry recorded just after the occultation with the same instrument (to establish the intensity ratio of the blended star to Triton). The two methods of photometric calibration agreed within their errors and to within 1% of the background level (Olkin 1996), which is consistent with there being no significant extinction in the region of Triton’s atmosphere probed by Lick (since the isothermal model assumes a clear atmosphere). From Voyager data, an intermittent haze is seen on Triton up to an altitude of 30 km and condensation clouds exist below 10-km altitude

(Pollack *et al.* 1990). Since most of the chords did not probe much below 30 km and none probed below 10 km, the lack of discernible extinction is consistent with Voyager observations.

For the infrared Tr148B lightcurve recorded at the 1.1-m telescope at Lick, the half-light radius and energy ratio had to be fixed (not fitted parameters) because of the low SNR. They were fixed at the weighted average of the half-light radius and energy ratio from the (eight) other Tr148A and Tr148B occultation lightcurves. For these data (Lick IR lightcurve of Tr148B), only the signal levels were fit, and then they were used to determine the intensity ratio of the two stars (described above). For the WIRO lightcurve, the background level and full-flux level were fixed and not fitted parameters. Fits of the WIRO data with the photometric parameters free gave inconsistent and unrealistic results, which is not surprising due to the non-photometric conditions during the observations. The full-flux level was determined from post-event photometry. To determine the background level, we used the intensity ratio of the Tr148B to Tr148A described above (4.19 ± 0.22).

We also performed separate immersion and emersion fits to the highest SNR lightcurves (see Table VIII), again excluding data within 20% of the midtime. With these separate fits, we can look at variations in atmospheric parameters with latitude. Figure 9 shows that the derived equivalent-isothermal temperature, pressure, and half-light radius do not vary significantly with latitude.

Our adopted results for the equivalent-isothermal atmosphere model of Triton are given in Table IX. They are the partial lightcurve fit results of Table VII, with the error in the adopted impact parameter factored into the errors in the fitted parameters and derived quantities.

IX. DISCUSSION

In this section, we address the issues raised in the Introduction: (1) Now that we have probed the altitude range 20–100 km of Triton’s atmosphere, how do the results compare with published models? (2) Can we detect atmospheric pressure change with varying insolation? (3) Does the structure of Triton’s lower atmosphere vary with location? We start with the question of spatial variation. We expect Triton’s atmosphere to be spherically symmetric because the vapor-pressure equilibrium should isothermally the surface by sublimation and condensation, and at the higher altitudes (575 km) the atmospheric densities at ingress and egress from the UVS occultation data are consistent to within 5% which is consistent with a spherically symmetric atmosphere, but not conclusive because of the small sample set (two points on the limb).

At the altitudes probed by the main drop and recovery of the lightcurves, (~ 30 –100 km), the atmosphere shows

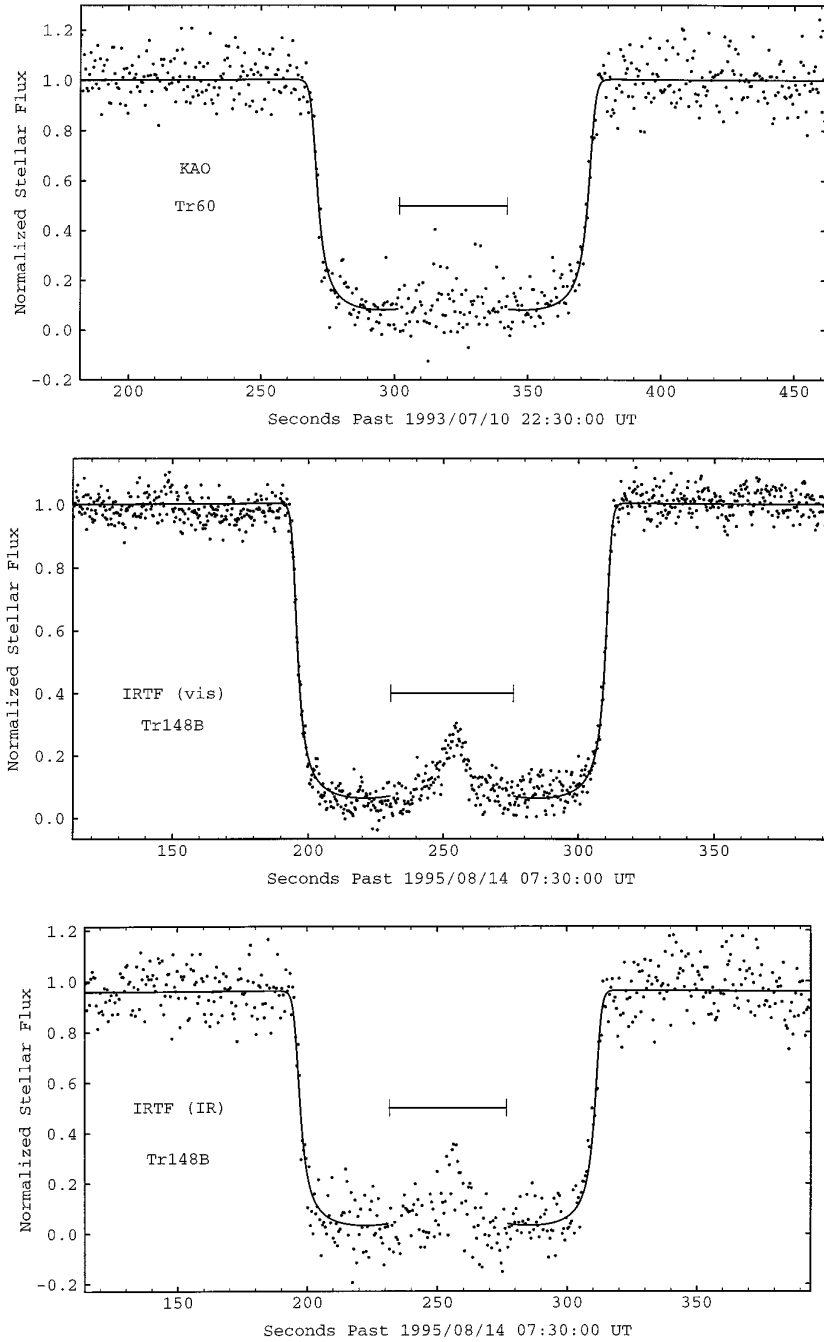


FIG. 8. Normalized Triton lightcurves and best-fitting model. The partial lightcurve fits did not include data within 20% of the occultation midtime, as indicated by the bar.

no significant asymmetry (Tables VIII, IX, Fig. 9) in scale height and half-light radius. Therefore, the atmospheric structure at 1400 km (where the atmospheric pressure is best determined) and at 1448.1 ± 1.8 km (the mean half-light radius) does not change with location; however, at the lowest altitude probed by these occultations (~ 20 km), the IRTF central-flash lightcurves are not consistent with

a symmetric atmosphere model. More on the inhomogeneity of the atmosphere at this level will be presented in Elliot *et al.* (1997). For the rest of the discussion, we use the higher altitude levels where we have established that the atmosphere is spherically symmetric to within the limited sampling and measurement error.

Next, we address temporal variability in Triton's atmo-

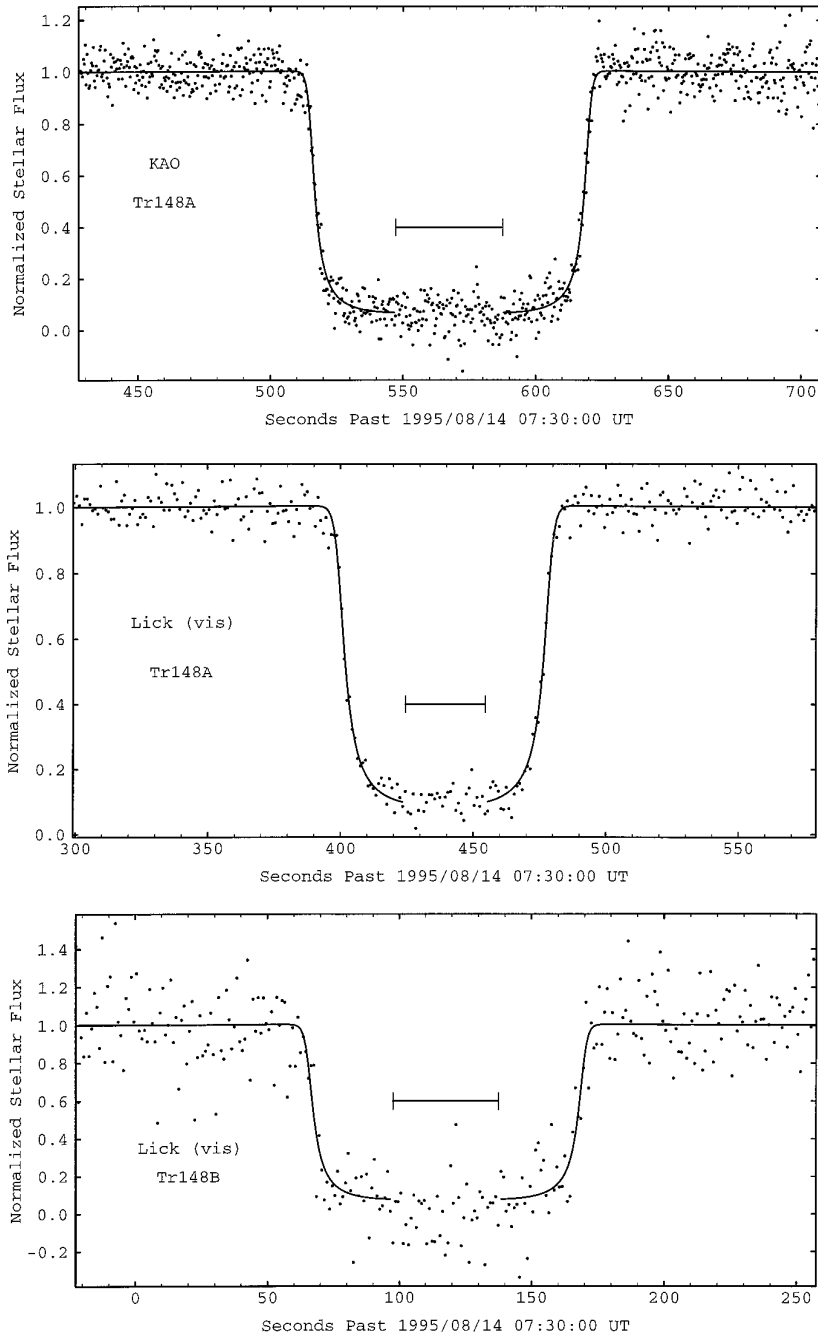


FIG. 8—Continued

sphere. Atmospheric change has been predicted to occur on Triton because of seasonal variations in insolation causing the surface temperature to change (Spencer 1990, Hansen and Paige 1992, Spencer and Moore 1992). The temperature of the surface ices should become isothermal by sublimation and conduction. A change in ice temperature will cause a change in atmospheric pressure due to vapor-pressure equilibrium. At the time of these observations, it was midsummer in Triton's southern hemisphere as the

subsolar point on Triton moved in latitude from -48° in 1993 to -49° in 1995. Unfortunately, due to the single-chord nature of the observations, the uncertainty in the pressure determined from the 1993 occultation is too large to provide a useful constraint on the pressure change between 1993 and 1995.

We cannot directly compare these occultation results to either the Voyager 2 RSS or UVS results because they probe a different altitude range; however, we can compare

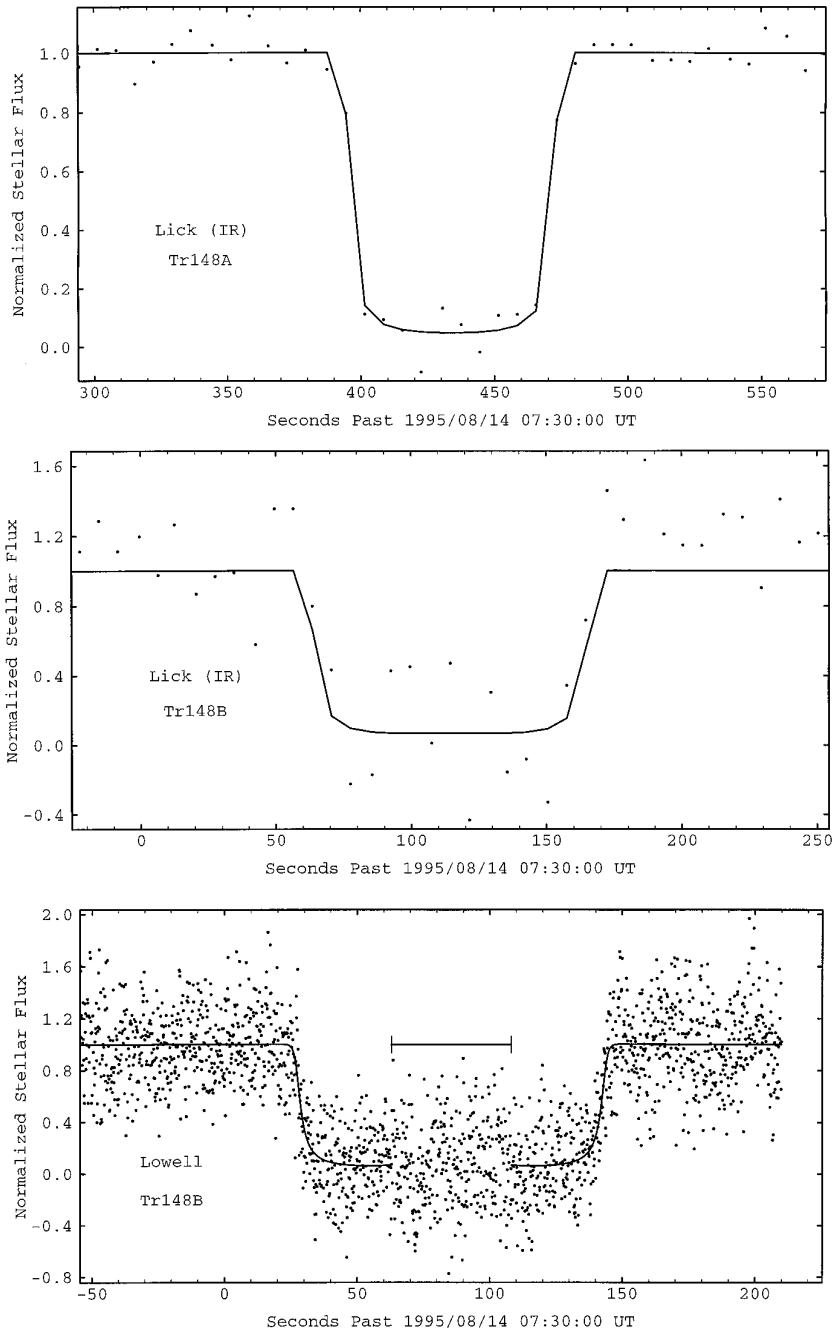


FIG. 8—Continued

the results of the lightcurve fits to radiative–thermal conduction models based on Voyager observations, such as the S96 model. The lightcurve fits give an equivalent-isothermal description of Triton’s atmospheric structure, but the S96 model does not. Therefore, to compare the two we need to convert the radiative–thermal conduction model to an equivalent isothermal one. This was done by constructing synthetic occultation lightcurves from the S96

model and then fitting the two-limb isothermal model to the synthetic lightcurves (see Table X). Three different synthetic lightcurves were constructed from the S96 model to simulate the three highest SNR lightcurves (using the impact parameter, shadow plane velocity, and integration time of the data sets). The atmospheric pressure at 1400 km derived from the equivalent-isothermal S96 model is almost a factor of 2 less than that from the occultation

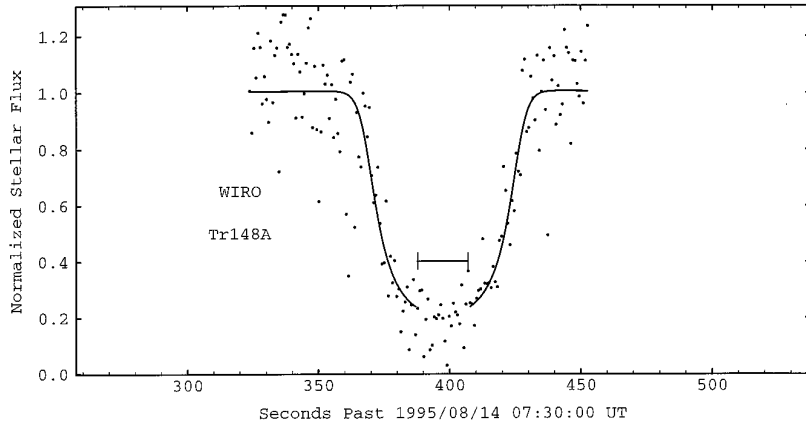


FIG. 8—Continued

data. The factor of 2 difference in atmospheric pressure derived from the occultation data and the equivalent-isothermal S96 pressure can be explained three different ways: (1) the atmospheric pressure has increased between 1989 and 1995, (2) the surface radius is larger than the value adopted in the isothermal model, and (3) the atmospheric structure at the microbar level is not properly modeled. Any combination of these could explain the observational results, each of which will be explained in turn. Most published seasonal change models do not predict an increase in atmospheric pressure of a factor of two or more from 1989 to 1995, but the basic parameters (e.g., thermal inertia

and N_2 inventory) that determine the seasonal transport of volatiles on Triton are not well known. All the Spencer and Moore (1992) models that show an increase in atmospheric pressure for 1989–1995 have a high thermal inertia.

The next explanation we consider for the pressure difference between the model atmosphere and the occultation data is an underestimate of the surface radius. To reconcile the factor of 1.8 difference in pressure at 1400 km and a scale height of ~ 20 km, the surface radius would have to be increased from 1352 to 1363 km. The surface radius of Triton was determined by Voyager 2 several different ways (with different data sets and different methods). From limb

TABLE VIII
Model Parameters from Fits of the Lightcurves (Immersion and Emersion Only)

Parameter	Light Curve	IRTF (vis)	KAO	Lick (vis)
		Tr148B	Tr148A	Tr148A
ρ_{\min} (km)		144.5 ± 27.3	680.2 ± 5.4	1086.6 ± 5.4
r_h (km)	immersion	$1446.1^{+3.4}_{-3.0}$	1446.5 ± 3.7	1450.2 ± 5.1
	emersion	$1449.5^{+3.4}_{-3.0}$	1447.6 ± 4.1	1448.1 ± 5.2
λ_h	immersion	73.6 ± 4.1	69.1 ± 6.0	70.3 ± 7.7
	emersion	75.7 ± 4.3	69.2 ± 7.0	65.7 ± 7.0
$H(r_h)$ (km)	immersion	19.6 ± 1.1	20.9 ± 1.8	20.6 ± 2.2
	emersion	19.1 ± 1.1	20.9 ± 2.1	22.0 ± 2.3
T_{iso} (K)	immersion	45.2 ± 2.5	48.1 ± 4.2	47.2 ± 5.2
	emersion	43.9 ± 2.5	48.0 ± 4.8	50.6 ± 5.4
P_{1400} (μbar)	immersion	$1.36^{+0.26}_{-0.21}$	$1.40^{+0.27}_{-0.25}$	$1.68^{+0.46}_{-0.40}$
	emersion	$1.63^{+0.33}_{-0.25}$	$1.48^{+0.30}_{-0.29}$	$1.54^{+0.40}_{-0.35}$

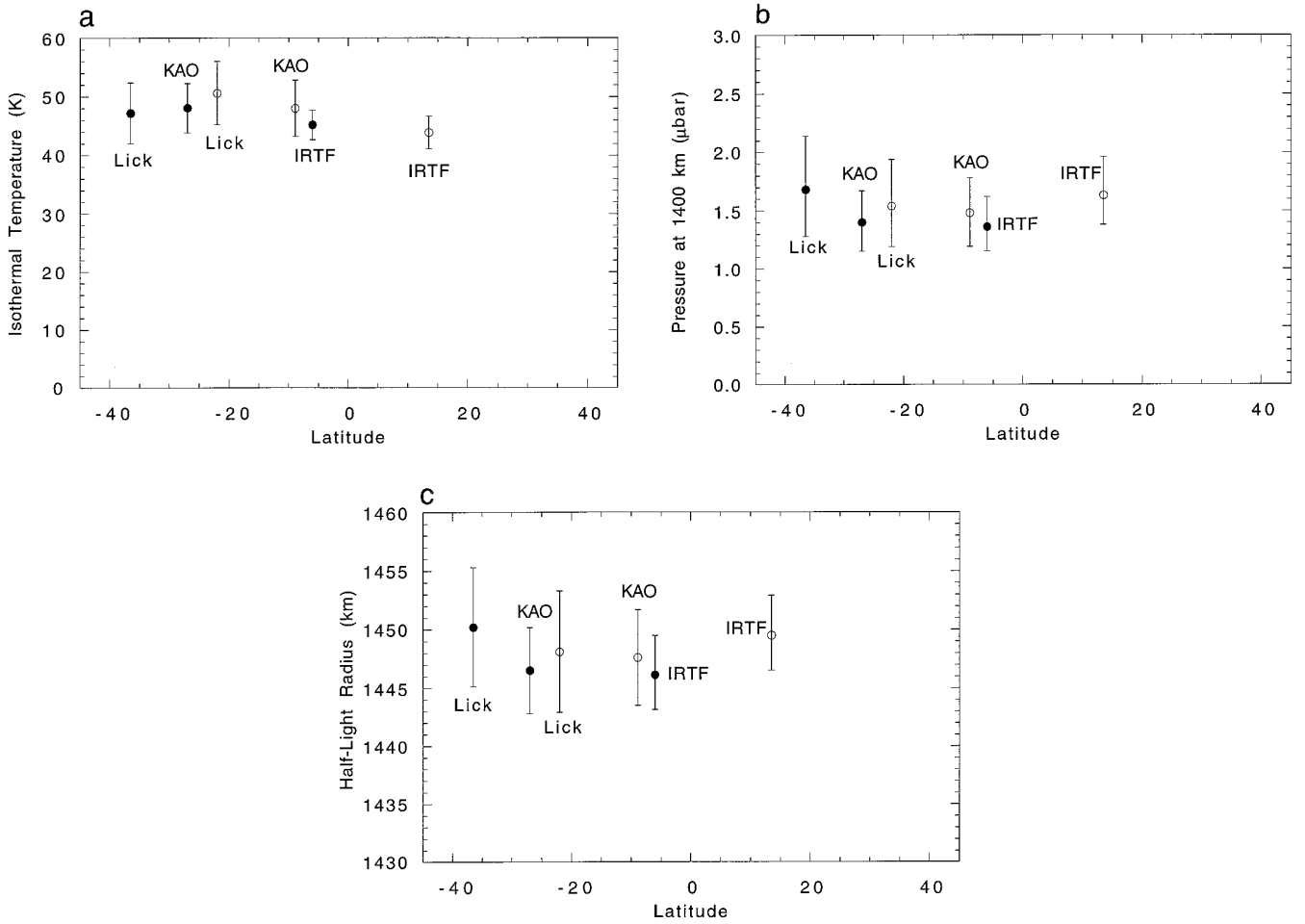


FIG. 9. Equivalent-isothermal temperature, atmospheric pressure at 1400-km radius, and half-light radius as a function of latitude on Triton. The separate immersion (solid circles) and emersion (open circles) fits of the highest SNR lightcurves probe Triton's atmosphere at six locations (from Table VIII). There is no significant trend in these quantities with latitude. This indicates that the asymmetry seen in the central flash does not extend to the fitted region of the lightcurves. Also, there is no signature of the 3% ellipticity of Triton's atmosphere determined in the elliptical-figure astrometric solution. This would be a change of ~ 40 km (or two scale heights) in the half-light radius. The data scatter less than expected for the error bars because a correlated error (the uncertainty in the impact parameter) is included in the error estimate.

TABLE IX
Adopted Equivalent-Isothermal Atmospheric Parameters

Parameter	KAO Tr60	IRTf (vis) Tr148B	IRTf (IR) Tr148B	KAO Tr148A	Lick (vis) Tr148A	Lick (vis) Tr148B	Lowell Tr148B	WIRO Tr148A
ρ_{\min} (km)	359 ± 133	144.5 ± 27.3	144.5 ± 27.3	680.2 ± 5.4	1086.6 ± 5.4	702.8 ± 27.3	261.0 ± 27.3	1304 ± 5.4
r_h (km)	$1451.0^{+38.9}_{-27.6}$	$1447.7^{+3.2}_{-2.8}$	$1442.9^{+4.9}_{-4.6}$	1447.0 ± 3.3	1449.2 ± 4.6	$1452.8^{+17.0}_{-16.8}$	$1453.5^{+7.9}_{-7.6}$	1461.1 ± 8.1
λ_h	$57.5^{+7.5}_{-7.1}$	74.6 ± 3.0	65.0 ± 7.3	69.1 ± 4.5	67.9 ± 5.2	60.3 ± 18.2	74.9 ± 14.8	51.8 ± 6.5
$H(r_h)$ (km)	25.2 ± 3.0	19.4 ± 0.8	22.2 ± 2.5	20.9 ± 1.4	21.4 ± 1.6	24.1 ± 7.2	19.4 ± 3.8	28.2 ± 3.6
T_{iso} (K)	$57.7^{+8.2}_{-7.6}$	44.5 ± 1.8	51.3 ± 5.8	48.1 ± 3.2	48.9 ± 3.7	54.9 ± 16.5	44.2 ± 8.7	63.6 ± 8.0
P_{1400} (μbar)	$1.8^{+7.9}_{-1.2}$	$1.4^{+0.3}_{-0.2}$	1.2 ± 0.3	1.4 ± 0.2	$1.6^{+0.4}_{-0.3}$	$1.9^{+1.8}_{-1.2}$	$2.0^{+0.9}_{-0.8}$	$2.8^{+0.9}_{-0.8}$

TABLE X
Comparison of Adopted Isothermal Atmospheric Parameters and
Atmospheric Models^a

Parameter	Light Curve	IRTF (vis) Tr148B	KAO Tr148A	Lick (vis) Tr148A
ρ_{\min} (km)		144.5 ± 27.3	680.2 ± 5.4	1086.6 ± 5.4
r_h (km)	data	$1447.7^{+3.2}_{-2.8}$	1447.0 ± 3.3	1449.2 ± 4.6
	S96	$1434.3^{+3.0}_{-2.5}$	1434.3 ± 2.6	1434.4 ± 4.1
λ_h	data	74.6 ± 3.0	69.1 ± 4.5	67.9 ± 5.2
	S96	$66.7^{+0.3}_{-0.2}$	66.7 ± 0.3	66.0 ± 0.4
$H(r_h)$ (km)	data	19.4 ± 0.8	20.9 ± 1.4	21.4 ± 1.6
	S96	21.49 ± 0.05	21.51 ± 0.05	21.72 ± 0.07
T_{iso} (K)	data	44.4 ± 1.8	48.1 ± 3.2	48.9 ± 3.7
	S96	50.3 ± 0.3	50.3 ± 0.3	50.8 ± 0.4
P_{1400} (μbar)	data	$1.4^{+0.3}_{-0.2}$	1.4 ± 0.2	$1.6^{+0.4}_{-0.3}$
	S96	0.8 ± 0.1	0.8 ± 0.1	$0.8^{+0.2}_{-0.1}$

^a Upper number from adopted fit; lower from fit of S96 model. The error in the parameters in the S96 model fits arise mainly from the uncertainty in the impact parameter.

measurements of Voyager imaging data, the surface radius was determined to be 1350 ± 5 km (Smith *et al.* 1989). This was refined by more extensive analysis of the imaging data by Davies *et al.* (1991), who established a surface radius of 1352.6 ± 2.4 km. Gurrola *et al.* (1992) reported that the chord length of the RSS occultation gives a radius of 1359.6 km with an uncertainty of 0.6Δ , where Δ is the cross-track uncertainty of the spacecraft. Coupling this with the UVS solar occultation gives 1351 ± 6 km, while coupling this with the UVS stellar occultation gives 1342 ± 8 km. Clearly, there is some uncertainty in the surface radius of Triton, but nevertheless most solutions would not be consistent with a radius of 1363 km. An underestimate of Triton's surface radius may not be the sole explanation for the pressure difference, although it could be part of the answer.

The last explanation for the larger surface pressure is that the radiative-thermal conduction model does not correctly describe Triton's atmosphere in the microbar region. The S96 model is based on RSS measurements that probed near the surface and UVS solar occultation data that probed much higher altitudes (500 km). The structure between these two regions is dominated by heat conduction down from the ionosphere and radiative transfer by CO and CH₄. If this model does not accurately describe the region probed by the occultation, we would expect the occultation data and radiative-conductive models to disagree (as they do).

probed by the occultation may not be correct: the strong thermal gradient predicted by a radiative-thermal conduction model (Strobel *et al.* 1996) may be present in our highest SNR data, but shifted to a colder temperature. The highest SNR data (IRTF vis) were fit using the power-law thermal gradient model adapted from Elliot and Young (1992) to include the far-limb flux contribution and resulted in a thermal gradient of 0.29 ± 0.25 K/km, (see Fig. 10) again the data within 20% of the midtime were excluded from the fit. This gradient is consistent with that from the S96 model at 1400 km (0.14 K/km) and the Krasnopolsky *et al.* (1993) model (~ 0.2 K/km). The temperature at 1400 km from the thermal-gradient model fit is 41.5 ± 5.2 K—colder than the S96 model (52.4 K) and consistent with the Krasnopolsky *et al.* (1993) model.

Consider the isothermal fit results to the occultation data in a different way. From the adopted fits (Table IX), the weighted average pressure at 1400-km radius in 1995 is 1.4 ± 0.1 μbar with an equivalent-isothermal temperature of 47 ± 1 K. If we assume the surface pressure is still 14 μbar (Gurrola 1995) as measured in 1989, then using the atmospheric pressure at 1400-km radius of 1.4 μbar , we would expect an equivalent-isothermal temperature of 53 K. This temperature is higher than either the measured temperature of the surface ice 38 K (Tryka *et al.* 1993) or the equivalent isothermal temperature derived from fitting the highest SNR occultation lightcurves (47 ± 1 K). We can reconcile these two temperatures (53 K and 47 K) if one of our assumptions is incorrect. The two assumptions

We have other evidence that the physics in the region

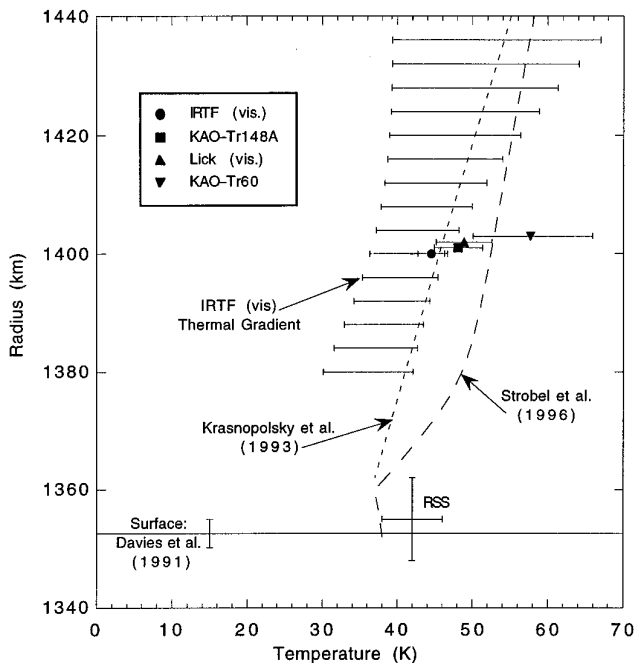


FIG. 10. Atmospheric temperature from the occultation data, two atmospheric models, and the Voyager RSS experiment. The RSS radius is from Tyler *et al.* (1989) and the RSS equivalent-isothermal temperature is from Gurrola (1995). The equivalent isothermal temperatures as determined from model fits are indicated by filled symbols. The isothermal temperatures refer to the range of atmosphere probed by the occultation and are indicated where the minimum fractional pressure and thermal gradient errors are near 1400 km. The 1σ temperature profile from the power-law thermal gradient model fit of the IRTF (vis) data is indicated by the bars.

were (1) the surface pressure is still $14 \mu\text{bar}$, and (2) the surface radius is 1352 km. We can reduce the 53 K by either increasing the atmospheric pressure or the surface radius. We have already addressed these possibilities.

X. CONCLUSIONS

We have fit an isothermal model to the 10 occultation lightcurves that constitute the complete set of ground-based stellar occultation data to date. Comparisons across the separate immersion and emersion lightcurve fits show no significant trend of temperature, pressure, or half-light radius with latitude. The consistency of the fitted half-light radius (1448.0 ± 1.8 km) and of the atmospheric pressure at 1400 km ($1.4 \pm 0.1 \mu\text{bar}$) indicates that the atmosphere is spherical at those levels within the errors and sampling limitations; however, we must keep in mind that the central-flash observations indicate the atmosphere is not spherically symmetric at the deepest levels probed, ~ 20 -km altitude.

We have also compared these occultation results to radi-

ative-thermal conduction models of Triton's atmosphere and have shown that the atmospheric pressure and temperature gradient predicted by radiative-thermal conduction models do not match that derived from the occultation data. The pressure at 1400 km is about a factor of 2 larger than that in the S96 model at the same radius, and the temperature derived from the occultation is consistently colder. The difference in atmospheric pressure could be due to seasonal change, but given the difference between the model and observed temperature, we believe at least some of the difference is a result of an inadequate model in the altitude range 30–100 km.

We look forward to regularly probing Triton's atmosphere with future stellar occultations to investigate the effects of seasonal change on Triton's tenuous atmosphere. Multi-chord occultation observations will allow us to better constrain seasonal change in atmospheric pressure. On 1997 July 18, Triton is predicted to occult the star Tr176 (McDonald and Elliot 1995). The star is brighter than any of the previously observed Triton occultation stars ($V = 12.53 \pm 0.02$, $J = 11.2 \pm 0.1$, $K = 10.5 \pm 0.2$; the V magnitude is courtesy of R. Stone at the USNO). It is unfortunate that the KAO has been shut down because the predicted track of this occultation is mostly over the Pacific Ocean.

ACKNOWLEDGMENTS

Without the measurements from the Carlsberg Automatic Meridian Circle (CAMC), we would not have attempted observations of the 1995 Triton occultations. Similarly, observations taken at the USNO Flagstaff Station were critical in the final prediction for both the Tr60 and Tr148 occultations. We thank the staff of the KAO for getting the airplane into the shadow path for the Tr60 observations (a difficult task with the daily prediction updates moving the track north) and for fitting the Tr148 occultation observation into their schedule. We thank the IRTF staff for assisting us in mounting our instrument on the optical port of NSF CAM and aiding our observations, W. Wild for supplying his observations from Yerkes, A. S. B. Shultz for flattening the LIRC2 observations, and A. Hancock for her work on the occultation lightcurves. We thank D. Strobel and X. Zhu for many helpful discussions and for providing their atmospheric model for comparison. We also thank the referees E. Gurrola and V. Krasnopolsky for many useful comments. This work was supported, in part, by NASA Grants NAGW-1494 at MIT, NAG 2-836 and NAGW-1912 at Lowell Observatory, and NAGW-1276 at WIRO. Support for this work was also provided by NASA through Grant GO-05825 from the Space Telescope Science Institute, which is operated by AURA, Inc., under NASA Contract NAS 5-26555.

REFERENCES

- Allen, C. W. 1973. *Astrophysical Quantities*. Athlone Press, London.
- Anderson, J. D., S. W. Asmar, J. K. Campbell, R. A. Jacobson, T. P. Kushner, E. R. Kurinski, E. L. Lau, and D. D. Morabito 1992. Gravitational parameters for Neptune and Triton. In *Proceedings, Neptune and Triton Conference, Tucson, Arizona*, p. 1.
- Baum, W. A., and A. D. Code 1953. A photometric observation of the occultation of σ Arietis by Jupiter. *Astron. J.* **58**, 108–112.

- Bosh, A. S., L. A. Young, J. L. Elliot, H. B. Hammel, and R. L. Baron 1992. Photometric variability of Charon at 2.2 μm . *Icarus* **95**, 319–324.
- Broadfoot, A. L., S. K. Atreya, J. L. Bertaux, J. E. Blamont, A. J. Dessler, T. M. Donahue, W. T. Forrester, D. T. Hall, F. Herbert, J. B. Holberg, D. M. Hunten, V. A. Krasnopolsky, S. Linick, J. I. Lunine, J. C. McConnell, H. W. Moos, B. R. Sandel, N. M. Schneider, D. E. Shemansky, G. R. Smith, D. F. Strobel, and R. V. Yelle 1989. Ultraviolet spectrometer observations of Neptune and Triton. *Science* **246**, 1459–1466.
- Buie, M. W., R. L. Millis, L. H. Wasserman, J. L. Elliot, S. J. Bus, E. W. Dunham, E. F. Young, W. B. Hubbard, D. M. Hunten, and W. K. Wells 1993. CCD camera occultation system. *Bull. Am. Astron. Soc.* **25**, 1115.
- Conrath, B., F. M. Flasar, R. Hanel, V. Kunde, W. Maguire, J. Pearl, J. Pirraglia, R. Samuelson, P. Gierasch, A. Weir, B. Bézard, D. Gautier, D. Cruikshank, L. Horn, R. Springer, and W. Shaffer 1989. Infrared observations of the neptunian system. *Science* **246**, 1454–1459.
- Cruikshank, D. P., and P. M. Silvaggio 1979. Triton: A satellite with an atmosphere. *Astrophys. J.* **233**, 1016–1020.
- Cruikshank, D. P., R. H. Brown, and R. N. Clark 1984. Nitrogen on Triton. *Icarus* **58**, 293–305.
- Cruikshank, D. P., T. L. Roush, T. C. Owen, T. R. Geballe, C. de Bergh, B. Schmitt, R. H. Brown, and M. J. Bartholomew 1993. Ices on the surface of Triton. *Science* **261**, 742–745.
- Davies, M. E., P. G. Rogers, and T. R. Colvin 1991. A control network of Triton. *J. Geophys. Res.* **96**, 15,675–15,681.
- Dunham, E. W. 1995. Optical instrumentation for airborne astronomy. In *Proceedings of the Airborne Astronomy Symposium on the Galactic Ecosystem: From Gas to Stars to Dust* (M. R. Haas, J. A. Davidson, and E. F. Erickson, Ed.), pp. 517–522. ASP, San Francisco.
- Dunham, E. W., R. L. Baron, J. L. Elliot, J. V. Vallerger, J. P. Doty, and G. R. Ricker 1985. A high-speed, dual-CCD imaging photometer. *Publ. Astron. Soc. Pacific* **97**, 1196–1204.
- Dunham, E. W., S. W. McDonald, and J. L. Elliot 1991. Pluto–Charon stellar occultation candidates: 1990–1995. *Astron. J.* **102**, 1464–1484.
- Elliot, J. L., and C. B. Olkin 1996. Probing planetary atmospheres with stellar occultations. In *Annual Review of Earth and Planetary Sciences* (G. W. Wetherill, Ed.), pp. 89–123. Annual Reviews Inc., Palo Alto, CA.
- Elliot, J. L., and L. A. Young 1992. Analysis of stellar occultation data for planetary atmospheres. I. Model fitting, with application to Pluto. *Astron. J.* **103**, 991–1015.
- Elliot, J. L., A. S. Bosh, M. L. Cooke, R. C. Bless, M. J. Nelson, J. W. Percival, M. J. Taylor, J. F. Dolan, E. L. Robinson, and G. W. van Citters 1993. An occultation by Saturn's rings on 1991 October 2–3 observed with the Hubble Space Telescope. *Astron. J.* **106**, 2544–2572.
- Elliot, J. L., R. G. French, E. Dunham, P. J. Gierasch, J. Veverka, C. Church, and C. Sagan 1977. Occultation of ϵ Geminorum by Mars. II. The structure and extinction of the martian upper atmosphere. *Astrophys. J.* **217**, 661–679.
- Elliot, J. L., J. A. Stansberry, C. B. Olkin, M. A. Agner, and M. E. Davies 1997. Triton's distorted atmosphere. *Science*. submitted.
- Gurrola, E. M. 1995. *Interpretation of Radar Data from the Icy Galilean Satellites and Triton*. Ph.D. thesis, Stanford University.
- Gurrola, E. M., E. A. Marouf, V. R. Eshleman, G. L. Tyler, and P. A. Rosen 1992. Analysis of Voyager radio occultation observations of Triton. In *Proceedings, Neptune and Triton Conference, Tucson, Arizona*, p. 28.
- Hansen, C. J., and D. A. Paige 1992. A thermal model for the seasonal nitrogen cycle on Triton. *Icarus* **99**, 273–288.
- Ingersoll, A. P. 1990. Dynamics of Triton's atmosphere. *Nature* **344**, 315–317.
- Jacobson, R. A., J. E. Riedel, and A. H. Taylor 1991. The orbits of Triton and Nereid from spacecraft and Earthbased observations. *Astron. Astrophys.* **247**, 565–575.
- Krasnopolsky, V. A., B. R. Sandel, F. Herbert, and R. J. Vervack 1993. Temperature, N_2 , and N density profiles of Triton's atmosphere: Observations and model. *J. Geophys. Res.* **98**, 3065–3078.
- McDonald, S. W., and J. L. Elliot 1992. Triton stellar occultation candidates: 1992–1994. *Astron. J.* **104**, 862–879.
- McDonald, S. W., and J. L. Elliot 1995. Triton stellar occultation candidates: 1995–1999. *Astron. J.* **109**, 1352–1362.
- Olkin, C. B. 1996. *Stellar Occultation Studies of Triton's Atmosphere*. Ph.D. thesis, Department of Earth, Atmospheric, and Planetary Sciences, Massachusetts Institute of Technology, Cambridge.
- Olkin, C. B., J. L. Elliot, S. J. Bus, S. W. McDonald, and C. C. Dahn 1996. Astrometry of single-chord occultations: Application to the 1993 Triton event. *Publ. Astron. Soc. Pacific* **108**, 202–210.
- Peck, E. R., and B. N. Khanna 1966. Dispersion of nitrogen. *J. Opt. Soc. Am.* **56**, 1059–1063.
- Pollack, J. B., J. M. Schwartz, and K. Rages 1990. Scatterers in Triton's atmosphere: Implications for the seasonal volatile cycle. *Science* **250**, 440–443.
- Seidelmann, P. K. 1992. Explanatory Supplement to the Astronomical Almanac.
- Shure, M., D. W. Toomey, J. T. Rayner, P. M. Onaka, and A. T. Denault 1994. *NSFCAM: A New Infrared Array Camera for the NASA Infrared Telescope Facility*. Instrumentation in Astronomy VIII, pp. 25–33. Kona, HI.
- Smith, B. A., L. A. Soderblom, D. Banfield, C. Barnet, A. T. Basilevsky, R. F. Beebe, K. Bollinger, J. M. Boyce, A. Brahic, G. A. Briggs, R. H. Brown, C. Chyba, S. A. Collins, T. Colvin, A. F. Cook II, D. Crisp, S. K. Croft, D. Cruikshank, J. N. Cuzzi, G. E. Danielson, M. E. Davies, E. De Jong, L. Dones, D. Godfrey, J. Goguen, I. Grenier, V. R. Haemmerle, H. Hammel, C. J. Hansen, C. P. Helfenstein, C. Howell, G. E. Hunt, A. P. Ingersoll, T. V. Johnson, J. Kargel, R. Kirk, D. I. Kuehn, S. Limaye, H. Masursky, A. McEwen, D. Morrison, T. Owen, W. Owen, J. B. Pollack, C. C. Porco, K. Rages, P. Rogers, D. Rudy, C. Sagan, J. Schwartz, E. M. Shoemaker, M. Showalter, B. Sicardy, D. Simonelli, J. Spencer, L. A. Sromovsky, C. Stoker, R. G. Strom, V. E. Suomi, S. P. Synott, R. J. Terrile, P. Thomas, W. R. Thompson, A. Verbiscer, and J. Veverka 1989. Voyager 2 at Neptune: Imaging science results. *Science* **246**, 1422–1449.
- Soderblom, L. A., S. W. Kieffer, T. L. Becker, R. H. Brown, A. F. Cook II, C. J. Hansen, T. V. Johnson, R. L. Kirk, and E. M. Shoemaker 1990. Triton's geyser-like plumes: Discovery and basic characterization. *Science* **250**, 410–415.
- Spencer, J. R. 1990. Nitrogen frost migration on Triton: A historical model. *Geophys. Res. Lett.* **17**, 1769–1772.
- Spencer, J. R., and J. M. Moore 1992. The influence of thermal inertia on temperatures and frost stability on Triton. *Icarus* **99**, 261–272.
- Strobel, D. F., and M. E. Summers 1995. Triton's upper atmosphere and ionosphere. In *Neptune and Triton* (D. P. Cruikshank, Ed.), pp. 1107–1148. Univ. of Arizona Press, Tucson.
- Strobel, D. F., X. Zhu, M. E. Summers, and M. H. Stevens 1996. On the vertical thermal structure of Pluto's atmosphere. *Icarus* **120**, 266–289.
- Trafton, L. 1984. Large seasonal variations on Triton. *Icarus* **58**, 312–324.
- Tryka, K. A., R. H. Brown, V. Anicich, D. P. Cruikshank, and T. C. Owen 1993. Spectroscopic determination of the phase composition and temperature of nitrogen ice on Triton. *Science* **261**, 751–754.

- Tyler, G. L., D. N. Sweetnam, J. D. Anderson, S. E. Borutzki, J. K. Campbell, V. R. Eshleman, D. L. Gresh, E. M. Gurrola, D. P. Hinson, N. Kawashima, E. R. Kursinski, G. S. Levy, G. F. Lindal, J. R. Lyons, E. A. Marouf, P. A. Rosen, R. A. Simpson, and G. E. Wood 1989. Voyager radio science observations of Neptune and Triton. *Science* **246**, 1466–1473.
- Yelle, R. V., J. I. Lunine, and D. M. Hunten 1991. Energy balance and plume dynamics in Triton's lower atmosphere. *Icarus* **89**, 347–358.
- Yelle, R. V., J. I. Lunine, J. B. Pollack, and R. H. Brown 1995. Lower atmospheric structure and surface–atmosphere interactions on Triton. In *Neptune and Triton* (D. P. Cruikshank, Ed.), pp. 1031–1105. Univ. of Arizona Press, Tucson.